Received: 22 March 2022 | Revised: 13 September 2022 | Accepted: 15 September 2022

DOI: 10.1002/nme.7127

RESEARCH ARTICLE

WILEY

An asynchronous variational integrator for the phase field approach to dynamic fracture

Zongwu Niu[1] | **Vahid Ziaei-Rad**[1,2] | **Zongyuan Wu**[1] | **Yongxing Shen**[1,3]

[1]University of Michigan – Shanghai Jiao Tong University Joint Institute, Shanghai Jiao Tong University, Shanghai, China

[2]Department of Environmental Informatics, Helmholtz Centre for Environmental Research – UFZ, Leipzig, Germany

[3]Shanghai Key Laboratory for Digital Maintenance of Buildings and Infrastructure, Shanghai, China

Correspondence
Yongxing Shen, University of Michigan – Shanghai Jiao Tong University Joint Institute, Shanghai Jiao Tong University, Shanghai 200240, China.
Email: yongxing.shen@sjtu.edu.cn

Funding information
National Natural Science Foundation of China, Grant/Award Number: 11972227; Natural Science Foundation of Shanghai, Grant/Award Number: 19ZR1424200

Abstract

The phase field approach is widely used to model fracture behaviors due to the absence of the need to track the crack topology and the ability to predict crack nucleation and branching. In this work, the asynchronous variational integrator (AVI) is adapted for the phase field approach of dynamic brittle fracture. The AVI is derived from Hamilton's principle and allows each element in the mesh to have its own local time step that may be different from others'. While the displacement field is explicitly updated, the phase field is implicitly solved, with upper and lower bounds strictly and conveniently enforced. In particular, two important variants of the phase field approach, the AT1 and AT2 models, are equally easily implemented. Several benchmark problems are used to study the performances of both the AT1 and AT2 models, and the results show that the AVI for the phase field approach significantly speeds up the computational efficiency and successfully captures the complicated dynamic fracture behavior.

KEYWORDS

asynchronous variational integrators, computational efficiency, dynamic fracture, phase field approach

1 | INTRODUCTION

Dynamic fracture refers to crack development processes accompanied by fast changes in applied loads and rapid crack propagation, where inertial forces play an important role during the evolution. Application examples of dynamic fracture include drop tests of electronic devices,[1] oil recovery,[2] and impact of automotive laminated glass.[3]

Dynamic fracture of solids has been extensively studied.[4-7] Over the past decades, various numerical methods[8] to simulate dynamic fracture have been proposed, which can be classified into two groups: discrete approaches and smeared-crack ones. A discrete approach explicitly describes the crack topology, such as the extended finite element method,[9] cohesive zone model,[10] element deletion method,[11] cracking element method,[12] and phantom nodes method,[13] just to name a few in the context of dynamic fracture. Conversely, a smeared-crack approach represents the crack by a smeared crack band, which includes the gradient damage model,[14] the thick level set approach,[15] and so on.

The regularized variational fracture method,[16] also called the phase field method for fracture, belongs to the group of smeared-crack approaches. It originates from Griffith's energetic theory and was developed based on the variational approach to brittle fracture by Francfort and Marigo.[17] The formulation solves crack problems by minimizing an energy functional that consists of the elastic energy, the external work, and the crack surface energy. This way, crack evolution is a natural outcome of the solution. The phase field method possesses the following advantages: (1) the crack evolves naturally and there is no need of a crack tracking algorithm; (2) there is no need of additional criterion for crack branching and

merging; (3) the implementation is straightforward even for complicated crack problems in 3D. These advantages facilitate its application for various fracture problems, such as shell fracture,[18] beam fracture,[19] and carbon dioxide fracturing.[20] For details about the implementation of this approach, we refer the reader to the work by Shen et al.[21]

For dynamic fracture, Borden et al.[22] combined the phase field method with isogeometric analysis with local adaptive refinement to simulate dynamic brittle fracture. Nguyen and Wu[23] presented a phase field regularized cohesive zone model for dynamic brittle fracture. Hao et al.[24,25] developed the formulations for high-speed impact problems for metals, accounting for volumetric and shear fracture.

However, the phase field model suffers from high computational cost partly because of the small critical time step, which, in turn, results from the necessary fine spatial discretization near the crack to resolve the regularization length scale. In order to overcome this challenge, various schemes to accelerate such computation have been proposed. Tian et al.[26] presented a multilevel hybrid adaptive finite element phase field method for quasi-static and dynamic brittle fracture, wherein the refinement is based on the crack tip identified with a certain scheme. Ziaei-Rad and Shen[27] developed a parallel algorithm on the graphical processing unit with a time adaptivity strategy to speed up the computation. Li et al.[28] proposed a variational h-adaption method with both a mesh refinement and a coarsening scheme based on an energy criterion. Engwer et al.[29] proposed a linearized staggered scheme with dynamic adjustments of the stabilization parameters throughout the iteration to reduce the computational cost.

In this work, we adapt the asynchronous variational integrator (AVI) to accelerate the computation for the phase field approach to dynamic fracture. The AVI is an instance of variational integrators. Variational integrators are a class of time integration algorithms derived from Hamilton's principle of stationary action and have the advantages of symplectic momentum conservation and remarkable energy (or Hamiltonian) behavior for long-time integration. In essence, they can be classified into synchronous variational integrators and asynchronous variational integrators. The former, such as central difference, requires all unknown variables to be solved with the same time step, taking into account the global requirement of stability and accuracy.

In contrast, the latter allows independent time steps for each term contributing to the action functional, effectively independent time steps for each element in the context of finite elements. This asynchrony allows the elements with smaller time steps to be more frequently updated. Moreover, the method may be made fully explicit and even in the implicit case, only assembly of the local reaction force vector and stiffness matrix instead of global ones is needed. For linear elastodynamics, the AVI was first introduced by Lew et al.,[30,31] and the stability and convergence of AVI have been proved by Fong et al.[32] and by Focardi and Mariano,[33] respectively. In addition, the AVI has been extended to the contact problem,[34] wave propagation,[35] and computer graphics.[36]

In the case of AVI for the phase field approach to fracture, a few adjustments need to be made. First and foremost, the overall Lagrangian is free of the time derivative of the phase field; hence solving the phase field is a local steady-state problem. More precisely, the coupled multi-field system is solved by employing a staggered scheme, in which the displacement and velocity fields are integrated with an explicit scheme while the phase field is the solution of an inequality-constrained optimization problem. In essence, the phase field of only one element is solved at a time, for which it is very convenient to enforce the inequality constraint compared to doing so for the entire domain. This feature allows implementing the AT1 variant[37] of the method with a similar cost to the more widely used AT2 variant,[16] the two variants differing in terms of the crack surface density function.

The AVI for the phase field approach has many advantages. First, the formulation is derived from the (discrete) Hamilton's principle and possesses a variational structure, which conserves the local symplectic momentum and possesses good global energy behavior of the system. More importantly, this formulation alleviates the high computational cost for certain problems such as those involving bi-materials or functionally graded materials, by allowing each element to have an independent time step only restricted by the respective elemental critical time step for stability. In addition, the formulation only needs to assemble the elemental (or patchwise) residual vector and tangent stiffness matrix and enforces the irreversibility condition on only one element instead of over the entire domain. These features render the proposed formulation highly efficient.

There are other asynchronous methods for dynamic fracture with the phase field. For example, Ren et al.[38] proposed an explicit phase field formulation where the mechanical field is solved with a larger time step while the phase field is updated with smaller sub-steps. Suh and Sun[39] presented a subcycling method to capture the brittle fracture in porous media, where the heat transfer between the fluid and solid constituents is solved with different time steps as integer multiples of each other. Note that the formulations in References 38 and 39 are not variational but obtained by directly discretizing the time-dependent mechanical and phase field differential equations, and hence may not enjoy the said advantages of variational integrators, that is, they may not preserve the symplectic and variational structure of the system.

The article is organized as follows. In Section 2, we briefly review the formulation of the phase field model for brittle fracture and introduce Hamilton's principle in the continuum Lagrangian framework. In Section 3, we present the asynchronous spacetime discretization scheme and derive the discrete Euler–Lagrange equations by discrete variational principle, then we present how to solve the mechanical field and phase field by a staggered scheme. In addition, we summarize the overall implementation of AVI for the phase field approach to fracture. In Section 4, we showcase four benchmark examples under dynamic loading for verification and examining the performance. Finally, we conclude this work in Section 5.

2 | FORMULATIONS

This section devotes to the formulation of a dynamic fracture phase field model through Hamilton's principle for an elastic body with possible cracks represented by a phase field.

2.1 | Hamilton's principle

Let $\Omega \subset \mathbb{R}^n$, $n = 2, 3$, be the domain occupied by the reference configuration of a body with possible cracks. Hamilton's principle states that the true trajectory of a body with prescribed initial and final conditions is the stationary point of the action functional with respect to arbitrary admissible variations. Here, we consider Ω with possible internal cracks during a specified time interval $t \in [t_0, t_f]$ with the action functional given by

$$S(\boldsymbol{u}, d) = \int_{t_0}^{t_f} L(\boldsymbol{u}, \dot{\boldsymbol{u}}, d)\ \mathrm{d}t, \tag{1}$$

where $\boldsymbol{u}(\boldsymbol{X}, t)$, $\boldsymbol{X} \in \Omega$, denotes the displacement field of the body, and $\dot{\boldsymbol{u}} = \mathrm{d}\boldsymbol{u}/\mathrm{d}t$ is the velocity field. The scalar field $d : \Omega \times [t_0, t_f] \to [0, 1]$ is called the phase field, which approximates possible sharp cracks in a diffusive way. Herein, the Lagrangian function is in the form

$$L(\boldsymbol{u}, \dot{\boldsymbol{u}}, d) = T(\dot{\boldsymbol{u}}) - V(\boldsymbol{u}, d) - \Gamma(d), \tag{2}$$

where $V(\boldsymbol{u}, d)$ is the potential energy, $\Gamma(d)$ is the crack surface energy, and

$$T(\dot{\boldsymbol{u}}) = \int_\Omega \frac{1}{2}\rho \dot{\boldsymbol{u}} \cdot \dot{\boldsymbol{u}}\ \mathrm{d}\Omega, \tag{3}$$

is the kinetic energy, where ρ is the initial mass density.

2.2 | Phase field approximation

In this subsection, we revisit the two versions of the phase field model as a basis for subsequent development. In the phase field model of fracture, the sharp crack surface is approximated by a scalar phase field d as shown in Figure 1. The range of this field d has to be between 0 and 1. In particular, our convention is such that the region with $d = 1$ represents the fully cracked state and that with $d = 0$ represents the pristine state of the material. Following Reference 16, the crack surface energy $\Gamma(d)$ in (2) is given by

$$\Gamma(d) = \int_\Omega g_c \gamma(d, \nabla d)\ \mathrm{d}\Omega, \tag{4}$$

where $g_c > 0$ is the critical crack energy release rate, and $\gamma(d, \nabla d)$ is the crack surface density per unit volume,

$$\gamma(d, \nabla d) = \frac{1}{4c_w}\left(\frac{w(d)}{\ell} + \ell |\nabla d|^2\right), \tag{5}$$

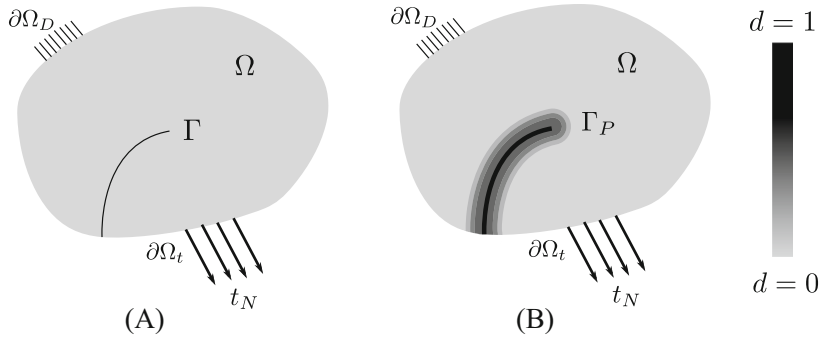

FIGURE 1 Body with an internal crack with: (A) A sharp crack; (B) a crack approximated by the phase field.

where $\ell > 0$ is the regularization length scale parameter, which controls the width of the transition region of the smoothed crack. Crack geometric function $w(d)$ and normalization constant $c_w = \int_0^1 \sqrt{w(d)}\, \mathrm{d}d$ are model dependent. Specifically, for the brittle fracture, classical examples are $w(d) = d^2$ and $c_w = 1/2$ for the AT2 model; and $w(d) = d$ and $c_w = 2/3$ for the AT1 model.[37] In addition, a notable difference between the AT2 and AT1 models is that the former gives rise to a more diffuse phase field profile while the latter generates a phase field profile with a narrow support near the crack.

The potential energy $V(\boldsymbol{u}, d)$ in (2) is expressed as

$$V(\boldsymbol{u}, d) = \int_\Omega \psi(\boldsymbol{\varepsilon}(\boldsymbol{u}), d)\, \mathrm{d}\Omega - \int_{\partial\Omega_t} \boldsymbol{t}_N \cdot \boldsymbol{u}\, \mathrm{d}A - \int_\Omega \boldsymbol{b} \cdot \boldsymbol{u}\, \mathrm{d}\Omega, \tag{6}$$

where ψ is the strain energy density, $\boldsymbol{t}_N : \partial\Omega_t \to \mathbb{R}^n$ is the prescribed traction boundary condition, and $\boldsymbol{b} : \Omega \to \mathbb{R}^n$ is the body force. The strain tensor is given by $\boldsymbol{\varepsilon} = (\nabla\boldsymbol{u} + \nabla\boldsymbol{u}^T)/2$, where $\nabla(\cdot)$ is the gradient operator with respect to $\boldsymbol{X}$.

Here we adopt a form for ψ that accounts for the unilateral constraint following Miehe et al.[40] which involves spectral decomposition of $\boldsymbol{\varepsilon}$. Other choices are, for example, the volumetric-deviatoric split by Amor et al.,[41] the micromechanics-informed model by Liu et al.,[42] and the model by Wu et al.[43] In the chosen formulation, the strain energy density takes the following form

$$\psi(\boldsymbol{\varepsilon}, d) = g(d)\psi_+ + \psi_-, \tag{7}$$

where $g(d) = (1 - d)^2$ is the degradation function, and ψ_+ and ψ_- are, respectively, the crack-driving and persistent portions of the strain energy density as

$$\psi_\pm(\boldsymbol{\varepsilon}) = \frac{\lambda}{2}\langle \mathrm{tr}\,(\boldsymbol{\varepsilon})\rangle_\pm^2 + \mu\, \mathrm{tr}\left(\boldsymbol{\varepsilon}_\pm^2\right), \tag{8}$$

where λ and μ are Lamé constants such that $\mu > 0$ and $\lambda + 2\mu > 0$, the Macauley bracket is defined as $\langle\cdot\rangle_\pm = (\cdot \pm |\cdot|)/2$, and

$$\boldsymbol{\varepsilon}_\pm = \sum_{a=1}^{3} \langle\varepsilon_a\rangle_\pm \mathbf{n}_a \otimes \mathbf{n}_a, \tag{9}$$

where $\{\varepsilon_a\}_{a=1}^3$ denote the principal strains, $\mathbf{n}_a$ are the corresponding orthonormal principal directions, and the operator $\otimes$ represents the dyadic product. Correspondingly, the Cauchy stress tensor is

$$\boldsymbol{\sigma}_\pm(\boldsymbol{\varepsilon}) = \frac{\partial\psi_\pm}{\partial\boldsymbol{\varepsilon}} = \lambda\langle \mathrm{tr}\,(\boldsymbol{\varepsilon})\rangle_\pm \mathbf{1} + 2\mu \sum_{a=1}^{3} \langle\varepsilon_a\rangle_\pm \mathbf{n}_a \otimes \mathbf{n}_a, \tag{10}$$

where $\mathbf{1}$ is the second-order identity tensor.

2.3 | Spatial discretization

In this subsection, we obtain the semi-discrete Lagrangian by discretizing the displacement field and the phase field with a finite element mesh $\mathcal{T}_h$ for Ω. Let η be the set of nodes of $\mathcal{T}_h$. The discretized fields take the following form

$$\boldsymbol{u}(\boldsymbol{X}) = \sum_{a\in\eta} N_a(\boldsymbol{X})\mathbf{u}_a, \quad d(\boldsymbol{X}) = \sum_{a\in\eta} N_a(\boldsymbol{X})d_a, \tag{11}$$

where $\mathbf{u}_a \in \mathbb{R}^n$ and $d_a \in \mathbb{R}$ are the displacement vector and phase field value at node $a \in \eta$, respectively, and N_a is the finite element shape function associated with node a.

The Lagrangian L may be decomposed as

$$L(\boldsymbol{u}, \dot{\boldsymbol{u}}, d) = \sum_{e\in\mathcal{T}_h} L_e\left(\mathbf{u}_e, \dot{\mathbf{u}}_e, \mathbf{d}_e\right), \tag{12}$$

where e is an element of the mesh $\mathcal{T}_h$, and $\mathbf{u}_e$, $\dot{\mathbf{u}}_e$, and $\mathbf{d}_e$ are the vectors containing the displacements, velocities, and phase field values of all the nodes of element e, respectively. The quantity L_e is given by

$$L_e\left(\mathbf{u}_e, \dot{\mathbf{u}}_e, \mathbf{d}_e\right) = T_e\left(\dot{\mathbf{u}}_e\right) - V_e\left(\mathbf{u}_e, \mathbf{d}_e\right) - \Gamma_e(\mathbf{d}_e), \tag{13}$$

where V_e and Γ_e are the elemental potential energy and elemental surface energy, respectively, and

$$T_e\left(\dot{\mathbf{u}}_e\right) = \frac{1}{2}\dot{\mathbf{u}}_e^T\mathbf{m}_e\dot{\mathbf{u}}_e, \tag{14}$$

is the elemental kinetic energy, where $\mathbf{m}_e$ is the diagonal element mass matrix. Hence, the space-discretized action is in the form

$$S\left(\{\mathbf{u}_e\}, \{\mathbf{d}_e\}\right) = \int_{t_0}^{t_f} \sum_{e\in\mathcal{T}_h} \left(\frac{1}{2}\dot{\mathbf{u}}_e^T\mathbf{m}_e\dot{\mathbf{u}}_e - V_e\left(\mathbf{u}_e, \mathbf{d}_e\right) - \Gamma_e(\mathbf{d}_e)\right) \mathrm{d}t, \tag{15}$$

where the curly braces $\{\cdot\}$ represent the collection of all components of all $e \in \mathcal{T}_h$ over the entire time span.

3 | ASYNCHRONOUS VARIATIONAL INTEGRATOR WITH THE FRACTURE PHASE FIELD

The main feature of the AVI is to assign different time steps to different elements of $\mathcal{T}_h$. The key idea is the stationarity of (15), a functional over space and time, which allows to divide the total Lagrangian into contributions from elemental terms which may possess independent time steps. For example, the smaller elements in the mesh may be updated a few times while the larger elements are held, according to either a preset schedule or a schedule determined on the fly.

In the context of fracture phase field in this work, the phase field is implicitly solved at the element level instead of at the global level, permitting more efficient solvers of inequality constraints.

In this section, we detail a phase field formulation and implementation for dynamic fracture through the AVI. The reader interested in the overall algorithmic implementation can directly go to Algorithm 2. In essence, we derive the proposed formulation from the discrete Hamilton's principle of stationary action with the fracture phase field incorporated. In addition, we adapt the reduced-space active set method to enforce the irreversibility constraint involved in the phase field problem.

3.1 | Asynchronous discretization

This subsection presents the discretization of the time domain through an asynchronous strategy. Such an asynchronous discretization allows each element to have an independent time step. As an example, Figure 2 shows the spacetime diagram of a three-element mesh with asynchronous time steps.

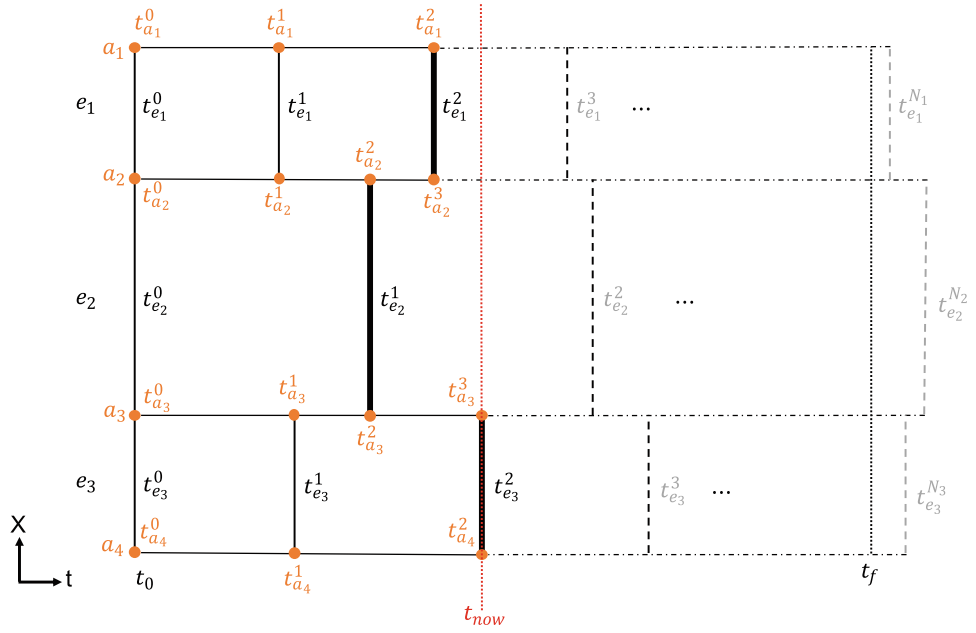

FIGURE 2 Asynchronous discretization of the time domain for a three-element mesh in the reference configuration. The entire update schedule follows the chronological order, that is, $\Theta = \{t^0_{e_1}, t^0_{e_2}, t^0_{e_3}, t^1_{e_1}, t^1_{e_3}, t^1_{e_2}, t^2_{e_1}, t^2_{e_3}, t^3_{e_1}, t^2_{e_2}, t^3_{e_3}, \dots\}$, where $t_{now} = t^2_{e_3}$ is the current time and e_3 is the current active element.

Here, we assign to the element $e \in \mathcal{T}_h$ the update schedule

$$\Theta_e = \left\{ t_0 = t_e^0 < t_e^1 < t_e^2 \cdots t_e^{N_e - 1} < t_f \le t_e^{N_e} \right\}. \tag{16}$$

At these instants, the displacements and velocities, and the phase field values of all nodes $a \in \eta(e)$ are updated, where $\eta(e)$ is the set of nodes of e. In addition, we define the discrete elemental displacements $\mathbf{u}_e^j \equiv \mathbf{u}_e(t_e^j)$ and the discrete elemental phase fields $\mathbf{d}_e^j \equiv \mathbf{d}_e(t_e^j)$ at $t_e^j \in \Theta_e$, and the entire update schedule of the mesh is

$$\Theta = \bigcup_{e \in \mathcal{T}_h} \Theta_e. \tag{17}$$

For simplicity, we assume that there are no coincident instants for any pair of elements except for the initial time, that is, $\Theta_e \cap \Theta_{e'} = \{t_0\}$ if $e \neq e'$. The general case with coincident update instants can be handled without much difficulty and will not change the results as long as elements with coincident instants are far away enough from each other. More discussions on the case of update coincidences for the adjacent elements are given in Appendix A.

Similarly, we also gather the schedule for node $a \in \eta$ as

$$\Theta_a = \bigcup_{e \ni a} \Theta_e = \left\{ t_0 = t_a^0 < t_a^1 < \cdots < t_a^{n_a - 1} < t_a^{n_a} \right\}. \tag{18}$$

We additionally define $\mathbf{u}_a^i \equiv \mathbf{u}_a(t_a^i)$, $d_a^i \equiv d_a(t_a^i)$, $t_a^i \in \Theta_a$, and the set of nodal displacements

$$\mathcal{U}_a = \left\{ \mathbf{u}_a^i \,:\, i = 0, 1, \dots, n_a \right\}, \ a \in \eta, \tag{19}$$

and the set of nodal phase fields

$$\mathcal{D}_a = \left\{ d_a^i \,:\, i = 0, 1, \dots, n_a \right\}, \ a \in \eta. \tag{20}$$

The triple $(\Theta, \mathcal{U}_a, \mathcal{D}_a)$ defines the discrete trajectory of the system. To solve for this triple, we write the discrete action sum as

$$S_{\text{dis}}(\Theta, \mathcal{U}_a, \mathcal{D}_a) = \sum_{e \in \mathcal{T}_h} \sum_{j=0}^{N_e - 1} L_e^j, \tag{21}$$

where $L_e^j \approx \int_{t_e^j}^{t_e^{j+1}} L_e \, \mathrm{d}t$.

This approximation can be realized by multiple schemes. In this article, we adopt one such that each node $a \in \eta$ follows a linear trajectory within the time interval $[t_a^i, t_a^{i+1}]$; consequently, the corresponding nodal velocities are constant in the said interval. Moreover, the potential energy and the crack energy terms are approximated with the rectangular rule using their values at t_e^{j+1}. Then the discrete Lagrangian is

$$\int_{t_e^j}^{t_e^{j+1}} L_e \, \mathrm{d}t \approx L_e^j = \sum_{a \in e} \sum_{t_a^i \in \left[t_e^j, t_e^{j+1}\right)} \frac{1}{2} m_{e,a} \left(t_a^{i+1} - t_a^i\right) \left\| \frac{\mathbf{u}_a^{i+1} - \mathbf{u}_a^i}{t_a^{i+1} - t_a^i} \right\|^2 - \left(t_e^{j+1} - t_e^j\right) \left(V_e\left(\mathbf{u}_e^{j+1}, \mathbf{d}_e^{j+1}\right) + \Gamma_e\left(\mathbf{d}_e^{j+1}\right)\right), \tag{22}$$

where $m_{e,a}$ is the mass matrix entry of node a contributed by element e and $\mathbf{d}_e^{j+1} \equiv \mathbf{d}_e(t_e^{j+1})$ is the elemental phase field vector. Finally, the discrete action sum (21) takes the following form

$$S_{\mathrm{dis}} = \sum_{a \in \eta} \sum_{i=0}^{n_a - 1} \frac{1}{2} M_a \left(t_a^{i+1} - t_a^i\right) \left\| \frac{\mathbf{u}_a^{i+1} - \mathbf{u}_a^i}{t_a^{i+1} - t_a^i} \right\|^2 - \sum_{e \in \mathcal{T}_h} \sum_{j=0}^{N_e - 1} \left(t_e^{j+1} - t_e^j\right) \left(V_e\left(\mathbf{u}_e^{j+1}, \mathbf{d}_e^{j+1}\right) + \Gamma_e\left(\mathbf{d}_e^{j+1}\right)\right), \tag{23}$$

where $M_a = \sum_{e, a \in \eta(e)} m_{e,a}$.

3.2 | Discrete variational principle

In this subsection, we derive the formulation of the AVI for the phase field approach to dynamic fracture using the discrete Hamilton's principle.[44] Taking the partial derivative of the discrete action sum (23) with respect to $\mathbf{u}_a^i$ follows

$$0 = \frac{\partial S_{dis}}{\partial \mathbf{u}_a^i} = \frac{\partial}{\partial \mathbf{u}_a^i} \left(\frac{1}{2} M_a \left(t_a^i - t_a^{i-1}\right) \left\| \frac{\mathbf{u}_a^i - \mathbf{u}_a^{i-1}}{t_a^i - t_a^{i-1}} \right\|^2 + \frac{1}{2} M_a \left(t_a^{i+1} - t_a^i\right) \left\| \frac{\mathbf{u}_a^{i+1} - \mathbf{u}_a^i}{t_a^{i+1} - t_a^i} \right\|^2 - \left(t_e^j - t_e^{j-1}\right) V_e\left(\mathbf{u}_e^j, \mathbf{d}_e^j\right) \right), \tag{24}$$

where $a \in \eta(e)$ such at $t_a^i = t_e^j$, which yields the discrete Euler–Lagrange equations

$$\mathbf{p}_a^{i+1/2} - \mathbf{p}_a^{i-1/2} = I_{e,a}^i = -\left(t_e^j - t_e^{j-1}\right) \frac{\partial V_e\left(\mathbf{u}_e^j, \mathbf{d}_e^j\right)}{\partial \mathbf{u}_a^i}, \tag{25}$$

where $I_{e,a}^i$ may be regarded as the impulse component of node $a \in e$ at the time $t_a^i = t_e^j$, and the discrete linear momentum is defined as

$$\mathbf{p}_a^{i-1/2} = M_a \frac{\mathbf{u}_a^i - \mathbf{u}_a^{i-1}}{t_a^i - t_a^{i-1}} = M_a \mathbf{v}_a^{i-1/2}. \tag{26}$$

Similarly, we take the partial derivative of (23) with respect to $\mathbf{d}_e^j$ as follows

$$0 = \frac{\partial S_{dis}}{\partial \mathbf{d}_e^j} = \frac{\partial}{\partial \mathbf{d}_e^j} \left[V_e\left(\mathbf{u}_e^j, \mathbf{d}_e^j\right) + \Gamma_e\left(\mathbf{d}_e^j\right) \right], \tag{27}$$

for element e at time t_e^j, then the phase field of element e are updated by

$$\mathbf{d}_e^j = \underset{\mathbf{d}_e^\star \le \mathbf{d}_e \le 1}{\arg\min} \left\{ V_e\left(\mathbf{u}_e^j, \mathbf{d}_e\right) + \Gamma_e\left(\mathbf{d}_e\right) \right\}, \tag{28}$$

where $\mathbf{d}_e^\star$ represents the phase field value of $\eta(e)$ at their most recent time of update; namely, for node $a \in \eta(e)$, at step i, $\mathbf{d}_e^\star$ contains the phase field value d_a^{i-1}. Note that normally in the same element e, $\mathbf{d}_e^\star$ may contain phase field values at different times. Here the stationarity condition (27) becomes a minimization in (28) since Γ_e is elliptic. The irreversibility constraint in (28) may be enforced in many ways, for which we have chosen the reduced-space active set strategy, to be discussed in Section 3.4.

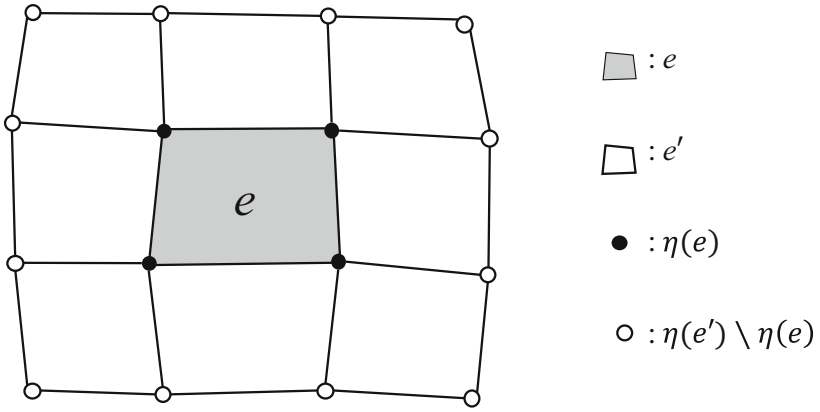

FIGURE 3 Diagram of a patch $\mathcal{T}_e$ that consists of the element e (gray element) and its adjacent elements $e' \in \mathcal{T}_e$ (white elements). At the beginning of an iteration for element e at time t_e^j for solving the phase field $\mathbf{d}_e^j$, the displacements $\mathbf{u}_e^j$ are known. Correspondingly, both the displacements $\mathbf{u}_{e'}^*$ and the phase fields $\mathbf{d}_{e'}^*$ of nodes in $\eta(e') \setminus \eta(e)$ (hollow nodes) assume their most recent values for the iteration.

Now, we consider an element $e \in \mathcal{T}_h$ with $\mathbf{u}_e^{j-1}$ and $\mathbf{p}_a^{i-1/2}$, $a \in \eta(e)$, known at time t_e^{j-1}, also known $\mathbf{d}_e^\star$, the provisional solution procedure is thus:

- For all $a \in \eta(e)$, solve $\mathbf{u}_a^i$ from (26): $\mathbf{u}_a^i = \mathbf{u}_a^{i-1} + (t_a^i - t_a^{i-1}) M_a^{-1} \mathbf{p}_a^{i-1/2}$.
- Solve $\mathbf{d}_e^j$ from (28).
- For all $a \in \eta(e)$, solve $\mathbf{p}_a^{i+1/2}$ from (25): $\mathbf{p}_a^{i+1/2} = \mathbf{p}_a^{i-1/2} - \left(t_e^j - t_e^{j-1}\right) \partial V_e \left(\mathbf{u}_e^j, \mathbf{d}_e^j\right) / \partial \mathbf{u}_a^i$.

3.3 | Reformulation for solving the phase field with element patches

The solution procedure mentioned above is variational; however, the results obtained with (28) show an unreasonable crack pattern (see Appendix B), hence we reformulate the constrained optimization problem (28) as follows. Essentially, we want to minimize $V + \Gamma$ with the newly obtained $\mathbf{u}_e^j$ (same as before) while the field values of all nodes not belonging to e frozen to their most recent values. To this end, we define the patch for element e

$$\mathcal{T}_e = \left\{ e' \in \mathcal{T}_h \,:\, \eta(e) \cap \eta(e') \neq \emptyset \right\}, \tag{29}$$

as shown in Figure 3. In this way, Equation (28) is modified to take into account the contributions of its neighboring elements

$$\mathbf{d}_e^j = \underset{\mathbf{d}_e^\star \le \mathbf{d}_e \le 1}{\arg\min} \sum_{\mathcal{T}_e} \left[V_e \left(\left\{ \mathbf{u}_{e'}^*, \mathbf{u}_e^j \right\}, \left\{ \mathbf{d}_{e'}^*, \mathbf{d}_e \right\} \right) + \Gamma_e \left(\left\{ \mathbf{d}_{e'}^*, \mathbf{d}_e \right\} \right) \right], \tag{30}$$

where the superscript $*$ represents the nodal values of $\eta(e') \setminus \eta(e)$ (hollow nodes in Figure 3) at their most recent time of update.

Based on the spatial discretization, the minimization problem (30) leads to the phase field residual of the element

$$(\mathbf{r}_e)_a := \int_{\mathcal{T}_e} \left[g'(d) \psi_+(\boldsymbol{\varepsilon}) N_a + \frac{g_c}{4 c_w} \left(\frac{w'(d) N_a}{\ell} + 2\ell \nabla d \cdot \nabla N_a \right) \right] \mathrm{d}\Omega, \quad a \in \eta(e), \tag{31}$$

where $g' = \mathrm{d}g/\mathrm{d}d$ and the tangent stiffness matrix of the element

$$(\mathbf{k}_e)_{aa'} := \int_{\mathcal{T}_e} \left[g''(d) \psi_+(\boldsymbol{\varepsilon}) N_a N_{a'} + \frac{g_c}{4 c_w} \left(\frac{w''(d) N_a N_{a'}}{\ell} + 2\ell \nabla N_a \cdot \nabla N_{a'} \right) \right] \mathrm{d}\Omega, \quad a, a' \in \eta(e). \tag{32}$$

For the detailed derivation of (31) and (32), the reader is referred to Shen et al.[21]

3.4 | Reduced-space active set method for irreversibility constraint

There are several approaches to impose the inequality constraints of the phase field when solving (30), such as the local history variable method,[40] the penalty method,[45] and the augmented Lagrangian method.[46]

In this work, we employ the reduced-space active set strategy[47] to ensure the phase field bounds $d \in [0, 1]$ and the irreversibility condition $\dot{d} > 0$. In the discrete setting, the phase field needs to satisfy the condition

$$0 \le d_a^{i-1} \le d_a^i \le 1, \quad \forall i = 1, 2, \dots, n_a \text{ and } a \in \eta(e). \tag{33}$$

Note that we solve this inequality-constrained optimization problem efficiently for only one element instead of for the entire domain. Then the solutions are determined by a mixed complementarity problem[48]

$$\begin{cases} d_a^{i-1} = d_a^i, & r_a \ge 0, \\ d_a^{i-1} \le d_a^i \le 1, & r_a = 0, \\ d_a^i = 1, & r_a \le 0, \end{cases} \tag{34}$$

where d_a^i is the nodal phase field at time $t_a^i = t_e^j$, and r_a is the phase field residual corresponding to node a. For each iteration, with $\mathbf{d}_e^\star$, $\mathbf{u}_e^j$, $\mathbf{d}_{e'}^*$, and $\mathbf{u}_{e'}^*$ of the patch at time t_e^j known, the phase field value of element e can be updated through Algorithm 1.

Algorithm 1. Reduced-space active set method for solving the phase field

Input: $\mathbf{d}_e^\star, \mathbf{u}_e^j, \mathbf{d}_{e'}^*, \mathbf{u}_{e'}^*, \forall e' \in \mathcal{T}_e$ and tol ▷ tol may be chosen differently at each occurrence
Output: $\mathbf{d}_e^j$

Compute $\mathbf{r}_e$ from (31) and initialize $\mathbf{d}_e^j = \mathbf{d}_e^\star$
▷ Let d_a^i and d_a^{i-1} denote the components of $\mathbf{d}_e^j$ and $\mathbf{d}_e^\star$ corresponding to node a, respectively, where d_a^i is the nodal phase field at time $t_a^i = t_e^j$. Initially $d_a^i = d_a^{i-1}$.
$\mathcal{A} = \left\{a \in \eta(e) : r_a > \text{tol or } \left(d_a^i = 1, r_a < -\text{tol}\right)\right\}, \mathcal{I} = \eta(e) \setminus \mathcal{A}$ ▷ All components of $\mathbf{d}_e^j$ are in either $\mathcal{A}$ or $\mathcal{I}$ at any time
while $\mathcal{I} \neq \emptyset$ **do**
  while $\|\mathbf{r}_\mathcal{I}\| > \text{tol}$ **do** ▷ $\{\}_\mathcal{I}$ is the component of $\{\}_e$ corresponding to nodes of $\mathcal{I}$
    Compute $\mathbf{k}_\mathcal{I}$ from (32), solve $\mathbf{d}_\mathcal{I} \leftarrow \mathbf{d}_\mathcal{I} - \mathbf{k}_\mathcal{I}^{-1}\mathbf{r}_\mathcal{I}$, and update $\mathbf{r}_\mathcal{I}$
  end while
  for $a \in \mathcal{I}$ **do**
    if $d_a^i > 1 + \text{tol}$ **then**
      Set $d_a^i \leftarrow 1$ and $\mathcal{A} \leftarrow \mathcal{A} \cup \{a\}, \mathcal{I} \leftarrow \mathcal{I} \setminus \{a\}$
    else if $d_a^i < d_a^{i-1} - \text{tol}$ **then**
      Set $d_a^i \leftarrow d_a^{i-1}$ and $\mathcal{A} \leftarrow \mathcal{A} \cup \{a\}, \mathcal{I} \leftarrow \mathcal{I} \setminus \{a\}$
    end if
  end for
  Compute $\mathbf{r}_\mathcal{A}$ from (31)
  if $\forall a \in \mathcal{A}$ satisfy (34) **then**
    return with $\mathbf{d}_e^j$
  else
    For each $a \in \mathcal{A}$ not satisfying (34), $\mathcal{I} \leftarrow \mathcal{I} \cup \{a\}, \mathcal{A} \leftarrow \mathcal{A} \setminus \{a\}$
  end if
end while

An explanation of Algorithm 1 is as follows. First, the phase field residual $\mathbf{r}_e$ is computed from (31) and the new phase field $\mathbf{d}_e^j$ is initialized with the old phase field $\mathbf{d}_e^\star$. Next, the set $\eta(e)$ is divided into an active set $\mathcal{A}$ and its complementary inactive set $\mathcal{I} = \eta(e) \setminus \mathcal{A}$ according to which case of (34) each node falls into, up to the given tolerance. If $\mathcal{I}$ is an empty set, then the procedure is returned with $\mathbf{d}_e^j$. Otherwise, the components of $\mathbf{r}_e$ corresponding to nodes of $\mathcal{I}$ need to be close enough to zero, up to a certain tolerance. For this purpose, Newton iteration is performed until convergence. After that,

the sets $\mathcal{A}$ and $\mathcal{I}$ are adjusted based on (33). This process of Newton iteration and adjustment of node sets is iterated until all nodes of $\mathcal{A}$ satisfy (34).

3.5 | Algorithmic implementation

This section focuses on the algorithmic implementation of the AVI for the phase field fracture. The overall pseudo-code is provided in Algorithm 2. The time step of each element is taken as a fraction of their critical time step and is computed by

$$t_{crit} = C_{CFL}\,\frac{2}{\omega_e}, \tag{35}$$

where C_{CFL} is taken as 0.6 and ω_e is the maximum natural frequency of the element, which is the square root of the maximum eigenvalue of the generalized eigenvalue problem $\mathbf{k}_e\mathbf{U} = \omega^2\mathbf{m}_e\mathbf{U}$. The time step of each element allows certain adaptivity, although we keep C_{CFL} constant in this work for simplicity.

Due to the asynchrony of the algorithm, we employ the priority queue[49] to keep track of the causality. The priority queue assigns each element a priority according to their next update time where the element to be updated at a sooner time has a higher priority. In other words, the priority queue ensures that all elements in the queue are ordered according to their next time to be updated, and the top element in the queue is always the one whose next update time is the closest to the current time in the future.

The implementation details are shown in Algorithm 2. First, the first time steps of all elements in the mesh are computed and pushed into the priority queue to establish the initial queue. Within each iteration, the priority queue pops an element (calls the active element) and its next update time. The nodal displacements, phase fields, and momenta of the active element are updated accordingly. Subsequently, the next update time of this element is computed and if this time is less than t_f, it is pushed into the priority queue. The algorithm continues until the priority queue is empty.

Algorithm 2. Algorithm of AVI for the phase field to fracture

Input: $\mathcal{T}_h,\ \eta,\ \Theta, Q = \emptyset$ and $\{\mathbf{u}_a^0,\ \mathbf{d}_e^0,\ \mathbf{p}_a^{1/2}\ |a \in \eta\}$
Output: $\mathbf{u}_a^i, \mathbf{d}_e^j, \mathbf{p}_a^{i+1/2}$, where $i,j = 1, 2, 3, \dots$, corresponding to Θ

Initialization: $\mathbf{u}_a \leftarrow \mathbf{u}_a^0,\ \mathbf{d}_e \leftarrow \mathbf{d}_e^0,\ \mathbf{p}_a \leftarrow \mathbf{p}_a^{1/2},\ \tau_a \leftarrow t_0$ for all $a \in \eta$
for all $e \in \mathcal{T}_h$ **do**
    $\tau_e \leftarrow t_0$
    Compute t_e^1 and push (t_e^1, e) into priority queue Q
end for
while Q is not empty **do**
    Extract next element: pop (t, e) from Q
    Compute displacements $\mathbf{u}_e$ with (26) and update node's time $\tau_a \leftarrow t$ for all $a \in \eta(e)$
    Compute the phase fields d_e with (30) following Algorithm 1
    if $t < t_f$ **then**
        Compute momentum $\mathbf{p}_a$ with (25) for all $a \in \eta(e)$
        Update element's time: $\tau_e \leftarrow t$
        Compute t_e^{next} and schedule e for next iterate: push (t_e^{next}, e) into Q
    end if
end while

4 | NUMERICAL EXAMPLES

In this section, we showcase four benchmark examples to demonstrate the ability of the proposed formulation in capturing the key features of dynamic fracture. In addition, we compare the computational costs and the energy conservation behavior of our approach for the AT1 and AT2 models. While all examples conducted here are two-dimensional, the proposed formulation is easy to be generalized to three dimensions. In particular, we use an unstructured mesh with first-order quadrilateral finite elements, which is refined along the potential crack paths.

A note on the post-processing is as follows. We sample the solution at a frequency of every 500,000 elemental iterations. For example, if the current time $t_{now} = t^2_{e_3}$ in Figure 2 happens to be a sampling time, then post-processing results are obtained using the most recent nodal displacement, velocity, and phase field values prior to t_{now}, that is, values at nodal times $t^2_{a_1}, t^3_{a_2}, t^3_{a_3}, t^2_{a_4}$ for the nodes shown. For example, the crack patterns to be plotted are obtained using the most recent phase field values prior to the sampling times. More accurate results can be obtained by interpolation using the values before and after the sampling time, which is not undertaken in this work for simplicity.

4.1 | Boundary tension test

In this section, a pre-notched rectangular plate loaded dynamically in tension is modeled. The geometry and boundary conditions are shown in Figure 4. A constant traction $\sigma^* = 1$ MPa is applied on the top and bottom edges throughout the simulation and the remaining boundary is traction free. This benchmark problem has been widely studied, for example by Song et al.[50] using the extended finite element method, by Nguyen[10] with the cohesive zone method, and by Borden et al.[22] with a synchronous phase field approach to fracture, as well as in experimental studies.[51,52] As described in Reference 51, a crack emerges at the notch tip and starts propagating to the right in a stable way. Over a certain distance, the main crack branches into two symmetrical sub-cracks and continue growing until it reaches the right surface.

The material used in this test is silica glass and its properties are listed in Table 1. A plane strain state with a unit thickness is assumed. The length scale parameter takes $\ell = 1 \times 10^{-3}$ m, which is small enough with respect to the specimen dimensions. Two different mesh levels are used: Mesh 1 with $h = 5 \times 10^{-4}$ m $= \ell/2$, and Mesh 2 with $h = 2.5 \times 10^{-4}$ m $= \ell/4$ in the refined region.

The final phase field results are shown in Figure 5. As seen, there is no significant difference of in the crack pattern between the AT2 and AT1 models. The crack branches at between 34 and 36 μs and reaches the right boundary at $t \approx 80$ μs. The upper crack branching angle is around 27.5°, which agrees well with the results in References 53 and 23. In addition, the bifurcation angle of the lower branch is slightly different from that of the upper one, which may be caused by the non-symmetric discretization of the mesh. This non-perfect symmetry was also observed by Ren et al..[38]

Figure 6A shows the evolution of the total crack tip velocity calculated by

$$v_{tip} = \frac{1}{g_c}\frac{\mathrm{d}\Gamma}{\mathrm{d}t}, \tag{36}$$

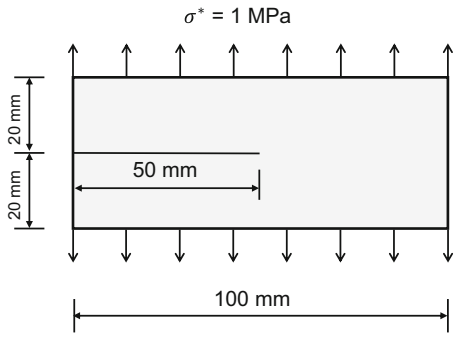

FIGURE 4 Geometry and boundary conditions of the boundary tension test, in which a pre-notched plate is under tension.

TABLE 1 Material properties for the numerical examples of Section 4.1 through Section 4.3.

Parameter	Symbol	Section 4.1	Section 4.2	Section 4.3
Material	-	Silica glass	Soda-lime glass	Maraging steel 18Ni(300)
Young's modulus (GPa)	E	32	72	190
Poisson's ratio	ν	0.2	0.22	0.3
Density (kg/m^3)	ρ	2450	2440	8000
Critical energy release rate (J/m^2)	g_c	3	3.8	2.213×10^4
Rayleigh wave speed (m/s)	v_R	2119	3172	2803

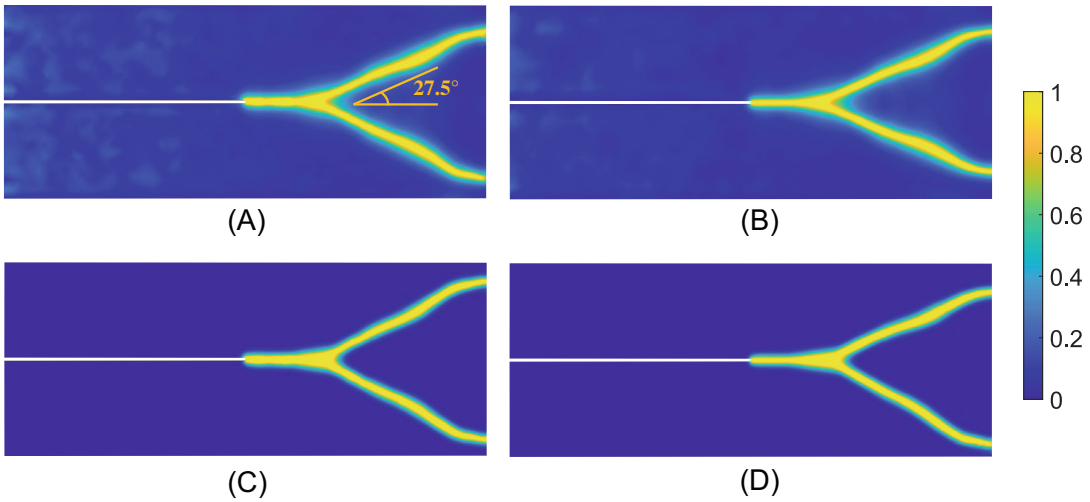

FIGURE 5 Phase field results of the test in Section 4.1. (A) AT2 with $h = l/2$; (B) AT2 with $h = l/4$; (C) AT1 with $h = l/2$; (D) AT1 with $h = l/4$

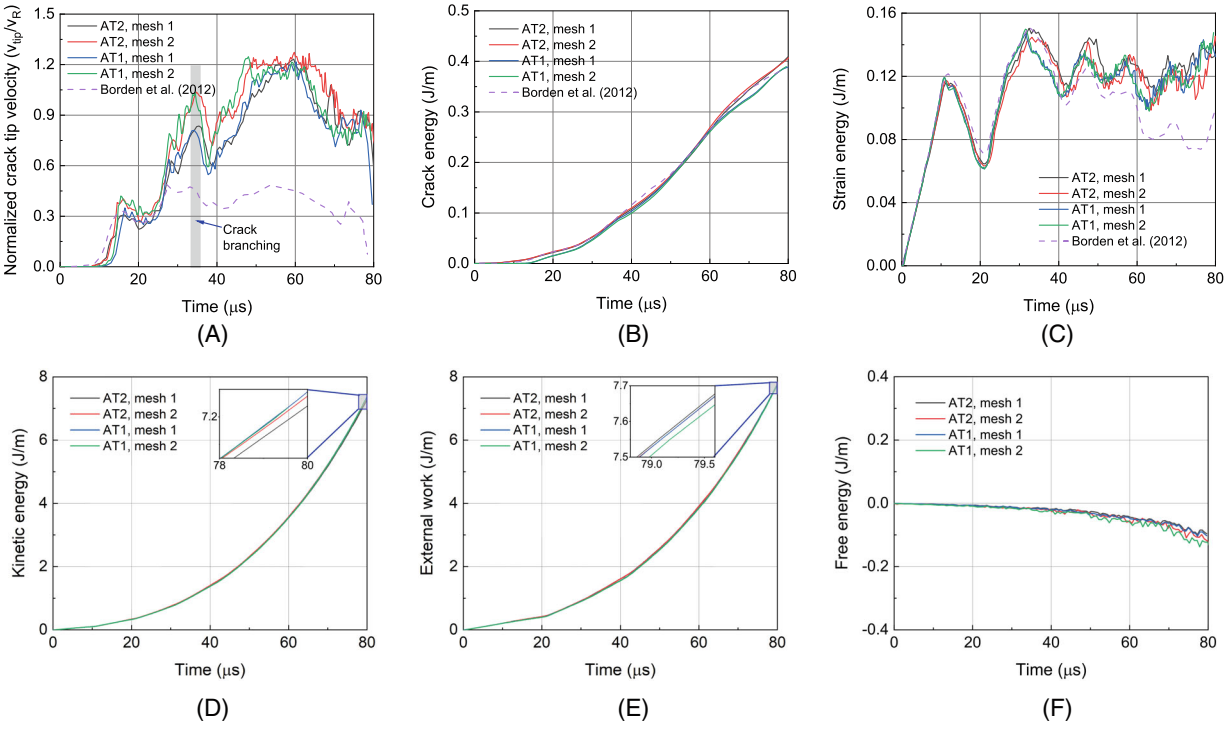

FIGURE 6 Results of the test in Section 4.1 compared with those of Borden et al.[22] Evolution of: (A) normalized total crack tip velocity; (B) crack energy $\Gamma(d)$; (C) strain energy; (D) kinetic energy $T(\dot{\boldsymbol{u}})$; (E) external work; and (F) free energy $T(\dot{\boldsymbol{u}}) + V(\boldsymbol{u}, d) + \Gamma(d)$. Note that for (A), the velocity result in Borden et al.[22] is only for one of the branches while it is the total velocity of both branches in this work. Here for (E) as well as for (B)–(D) the results are obtained by sampling, see the text for more details. It can be seen that the free energy is 1.32% of the external work at the end, indicating the conservation of energy.

and normalized by the Rayleigh wave speed. In particular, the derivative is obtained by comparing the values of Γ at consecutive sampling times. It is observed that at the beginning, a single main crack propagates to the right with a speed of less than 60% of the Rayleigh wave speed. Then, the main crack branches into two sub-cracks and in this respect the total crack tip velocity of both branches is plotted, which is still less than 60% of twice the Rayleigh wave speed. Therefore, whether before or after the branching emerges, the velocity is within a reasonable range. Moreover, the overall propagation speed during the evolution is in good agreement with the results reported by Borden et al.[22] Note that the velocity of Borden et al.[22] is only for one of the branches while it is the total velocity of both branches in this work.

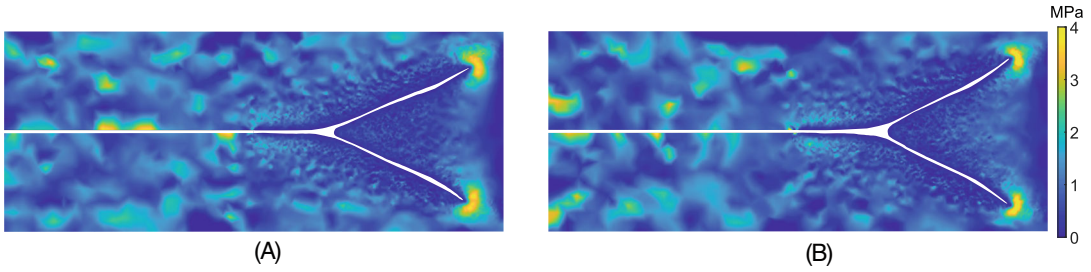

FIGURE 7 Maximum principal stress of the test in Section 4.1 with Mesh 1 at $t = 70\ \mu$s, where the region $d > 0.9$ is removed. (A) AT2; (B) AT1

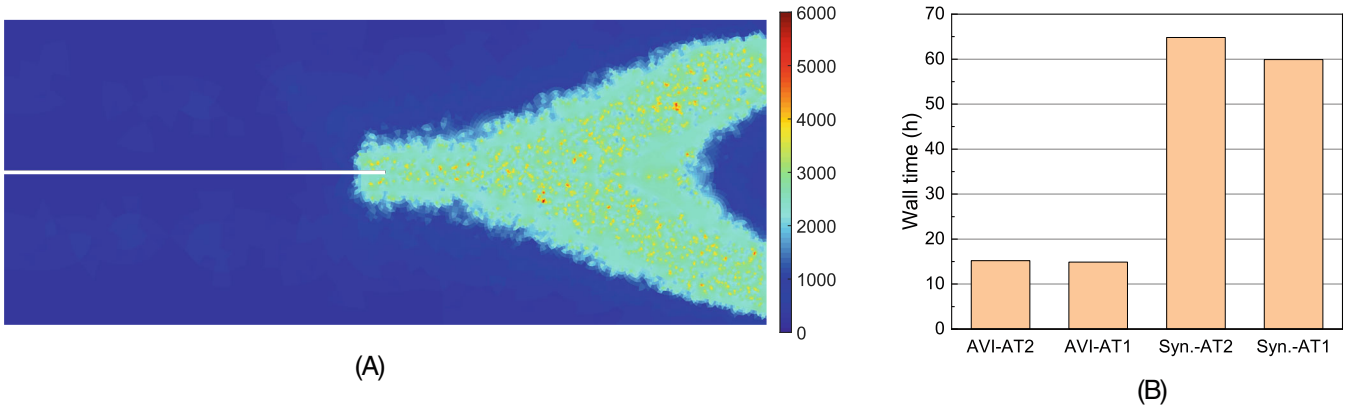

FIGURE 8 The performance indicators of the tests in Section 4.1 with Mesh 1: (A) Number of updates per element; and (B) wall time corresponding to $t_f = 80$ μs, where "Syn." represents the results of a synchronous method (central difference).

Figure 6B–D present the evolution of the crack surface energy, the strain energy, and the kinetic energy, respectively. The crack surface energy monotonically increases as expected due to the unilaterality of the phase field. In addition, the strain energy evidently shows the periodic oscillation at the beginning and this trend gradually weakens with crack evolution, because the stress wave is reflected at the boundaries and cracks, and interacts with itself.

Figure 6E shows the evolution of the external work, which is calculated from the second term on the right hand side of Equation (6). It is clear that the kinetic energy accounts for most of the energy converted from external work.

Figure 6F shows the evolutions of the free energy $T(\dot{\boldsymbol{u}}) + V(\boldsymbol{u}, d) + \Gamma(d)$. The free energy is negative and its magnitude is only 1.32% of the external work at the end. This small negative numbers demonstrate that the method possesses remarkable energy conservation property and is energetically stable.

Figure 7 shows the maximum principal stress with Mesh 1 at $t = 70$ μs. Therein, stress concentration is clearly seen at the crack tips and the results are in good agreement with those in Reference 54.

Figure 8A shows the number of updates per element for Mesh 1. By construction, the elements near the cracks are updated more frequently than those far away from the cracks. Figure 8B shows the wall time corresponding to $t_f = 80$ μs for the AVI and a synchronous method (central difference). The simulations are conducted using an in-house MATLAB code on a personal computer with Intel(R) Core(TM) i7-6700 CPU @ 3.40GHz and 16.0 GB RAM. The results indicate that the AVI for both AT2 and AT1 models take similar computational time. In addition, the computational efficiency of the AVI is approximately four times that of the synchronous method.

Table 2 collects statistics of the computational cost for the example at hand. As a platform-independent indicator, the number of updates of each element throughout the simulation for each case is counted. The second, third, and fourth columns represent the minimum, maximum, and median numbers of updates among the elements, respectively. The fifth column is the total numbers of updates for all elements of AVI. The sixth column is the total numbers of updates of synchronous integration, where the data is estimated by assuming the global critical time step is used for the same time interval $[t_0, t_f]$. As shown, the total numbers of AVI updates is approximately 31% of those of a synchronous

TABLE 2 Numbers of elemental updates for the test in Section 4.1 during the entire simulation.

Mesh	Minimum	Maximum	Median	AVI total[a]	Synchronous integration (estimated)[b]
Mesh 1	178	5983	2106	27,400,002	86,382,554
Mesh 2	160	10,150	3440	62,285,189	201,051,200

[a]Total numbers of the elements involved in the update of the mechanical field and phase field.
[b]This column of data is estimated by assuming the global critical time step is used throughout the computation for the same desired time interval $[t_0, t_f]$.

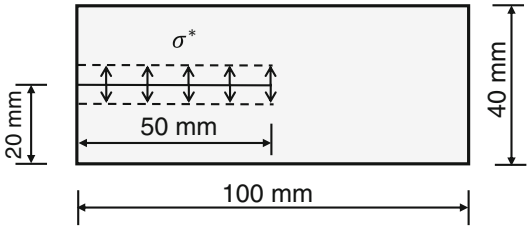

FIGURE 9 Geometry and boundary conditions for the dynamic CT test.

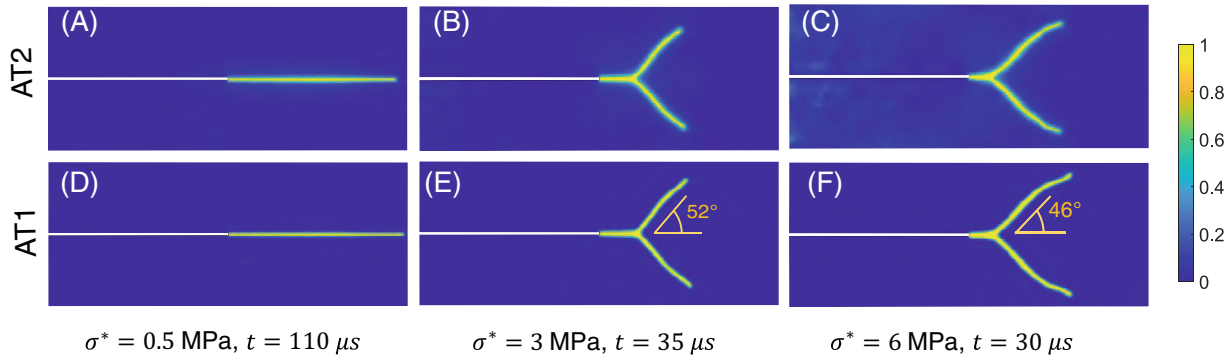

FIGURE 10 Phase field results of the test in Section 4.2 under different loads.

integration. Considering that it is even more costly to implicitly solve for the phase field with a synchronous method per time step, the data in Table 2 indicates that the proposed scheme effectively reduces the computational cost compared with a synchronous method.

4.2 | Compact tension test

In this section, we investigate a series of dynamic loads applied on pre-crack surfaces as the compact tension (CT) test. The geometry and boundary conditions are shown in Figure 9. Three different constant normal tractions $\sigma^* = \{0.5, 3, 6\}$ MPa are applied on the pre-crack surfaces. This benchmark problem has been studied by Bobaru and Zhang[55] using peridynamics and Mandal et al.[56] with a synchronous phase field approach.

The material is assumed to be soda-lime glass, whose properties are given in Table 1. Plane strain state is assumed. The length scale parameter $\ell = 5 \times 10^{-4}$ m and the mesh size $h = 2.5 \times 10^{-4}$ m $= \ell/2$ in the refined region are used for all cases. Figure 10 shows the phase field results for the CT test. For $\sigma^* = 0.5$ MPa, a straight crack without branching is obtained. For larger values of σ^* crack branching is observed and the branching location moves to the left with the increase of σ^*. The crack branching happens at around 17.3 and 9.2 μs, and the branching angles are 52° and 46° for $\sigma^* = 3$ and 6 MPa, respectively. Also, there is no significant difference of the crack patterns between the AT2 and AT1 models for the same load. Moreover, the crack patterns, branching instants, and branching angles are all in good agreement with the results reported in Reference 56.

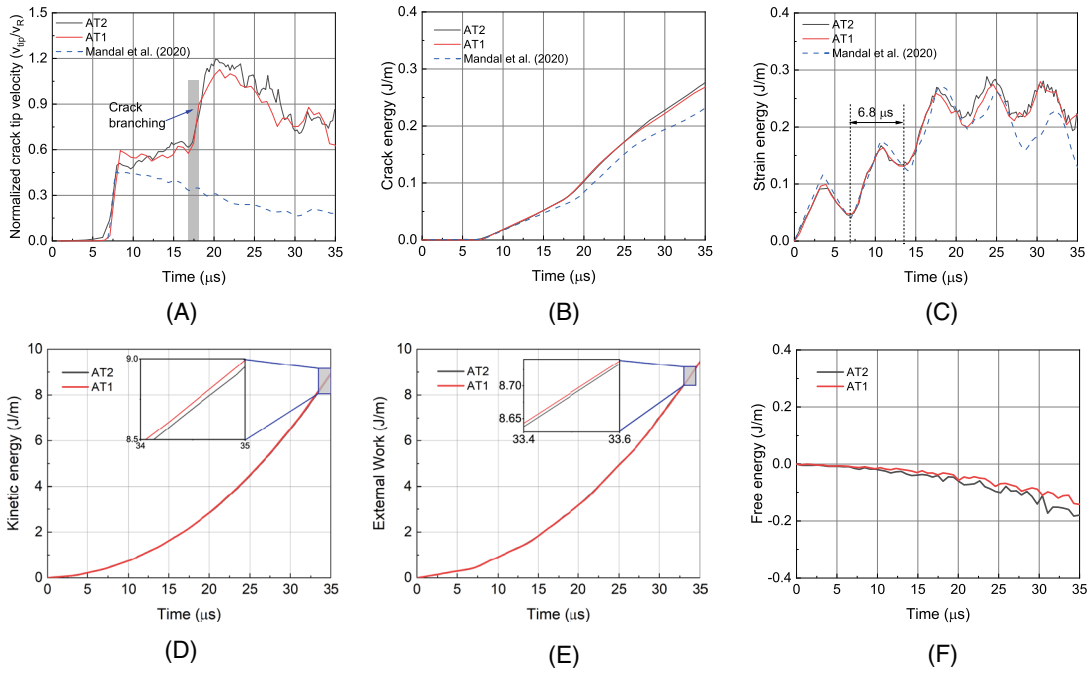

FIGURE 11 Results of the test in Section 4.2 with $\sigma^* = 3$ MPa compared with Mandal et al.[56] Evolution of: (A) Normalized total crack propagation velocity. Note that the velocity of Mandal et al.[56] is only for one of the branches while our result is the total velocity of both branches; (B) Crack energy; (C) strain energy; (D) kinetic energy; (E) external work; and (F) free energy. The free energy is only 1.69% of the external work, which indicates the conservation of energy.

Figure 11A illustrates the evolution of the normalized total crack tip velocity of CT test for $\sigma^* = 3$ MPa. Like the case of Figure 6A, a main crack propagates to the right with an increasing speed less than 60% of the Rayleigh wave speed. Then, then main crack branches into two sub-cracks and the total speed is still less than 60% of twice the Rayleigh wave speed. Note that the velocity of Mandal et al.[56] is only for one of the branches while our results are the total velocity of both branches. Figure 11B shows the evolution of the crack energy, and the results of both models are slightly higher than the result reported by Mandal et al.[56] Figure 11C shows the evolution of the strain energy. An interesting observation is that the curve presents a periodic oscillation with a period of approximately 6.8 μs, which can be explained as follows. During the process, the stress waves propagate from the crack to the top and bottom boundaries and then are reflected until they meet the crack again. The time it takes the stress wave to travel a round trip can be estimated by $l/v_D = 6.89$ μs, where $l = 40$ mm is twice the half-width of the specimen and $v_D = 5800$ m/s is the dilatational wave speed of soda-lime glass. This process is repeated, and hence the periodicity. Figure 11D,E show the evolution of the kinetic energy and the external work, both of which monotonically increase. Figure 11F shows the free energy of the AT2 and AT1 model during the evolution. As we can see, the magnitude of the free energy only accounts for 1.69% of the external work, which indicates the conservation of energy.

Figure 12 shows the maximum principal stress for $\sigma^* = 3$ and 6 MPa, respectively. Therein, stress concentration is clearly seen at the crack tips.

Figure 13A shows the number of updates per element with the mesh of the case $\sigma^* = 3$ MPa. Like the previous example, the elements in the refined region are updated more frequently while those without refinement are updated less frequently. Figure 13B shows the wall time corresponding to $t_f = 35$ μs of the AVI and a synchronous method for both models. As can be seen, the AVI takes one third time of a synchronous method.

4.3 | The Kalthoff-Winkler test

This section studies the Kalthoff-Winkler experiment in which an edge-cracked plate is under impact velocity. Due to symmetry, only half of the plate is considered. The geometry and boundary conditions are shown in Figure 14. In the experiment,[57,58] the brittle failure mode with a crack propagating at about 70° was observed at a certain impact speed,

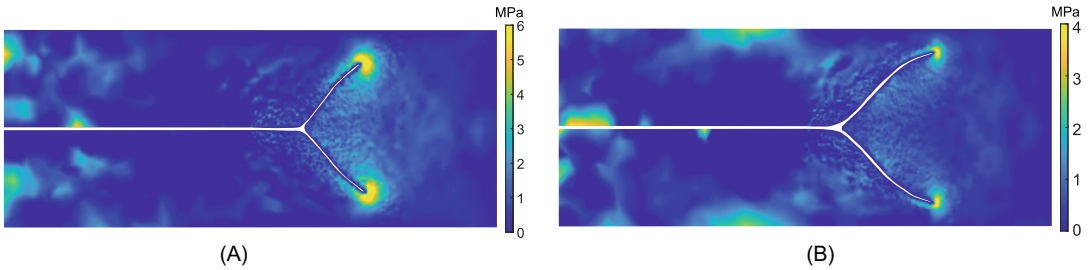

FIGURE 12 Maximum principal stress of the test in Section 4.2. (A) $\sigma^* = 3$ MPa, $t = 35$ μs; (B) $\sigma^* = 6$ MPa, $t = 30$ μs

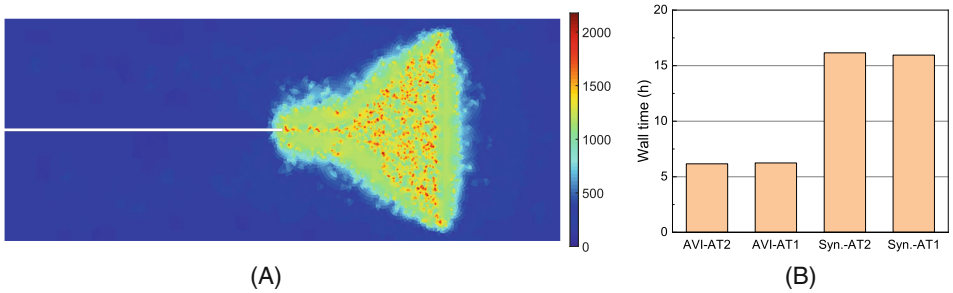

FIGURE 13 The performance indicators of the tests in Section 4.2 with the mesh of the case $\sigma^* = 3$ MPa: (A) Number of updates per element; and (B) wall time corresponding to $t_f = 35$ μs.

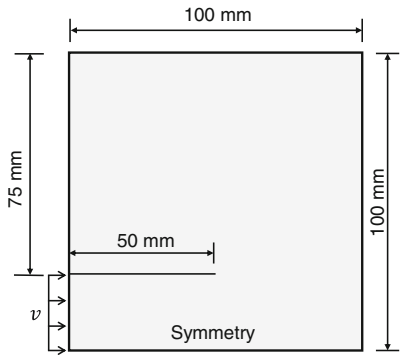

FIGURE 14 Geometry and boundary conditions of the Kalthoff test, where $v = 16.5$ m/s.

and the relevant numerical results were reported by other researchers using the extended finite element method,[50] peridynamics,[59] and the gradient damage method.[14]

The material is maraging steel 18Ni(300), whose properties are given in Table 1. A plane strain state is assumed. The length scale parameter $\ell = 3.9 \times 10^{-4}$ m and two different meshes are used: Mesh 1 with size $h = 1.95 \times 10^{-4}$ m $= \ell/2$ and Mesh 2 with $h = 9.75 \times 10^{-5}$ m$= \ell/4$ in the refined region.

Figure 15 shows the final phase field patterns at $t = 87$ μs for different meshes and models. The crack propagates at 25.5 μs and with an angle of about 67° with the horizontal line, which is in good agreement with the experimental results[57] and the numerical results using the phase field method.[60,61]

Figure 16A presents the evolution of the normalized crack tip velocity of the Kalthoff test. The velocity results here are almost two times that reported by Liu et al.[54] The differences in crack tip velocity may be caused by the different post-processing methods, where Reference 54 employed an alternative method that is different from ours by Equation (36), to be discussed later. Figure 16B shows the evolution of the crack energy calculated by (4), which agrees well with the numerical results in Reference 46. In addition, the crack energy of the AT2 model is a little higher than the AT1 model for both meshes. Figure 16C,D show the evolution of the strain energy and kinetic energy, respectively,

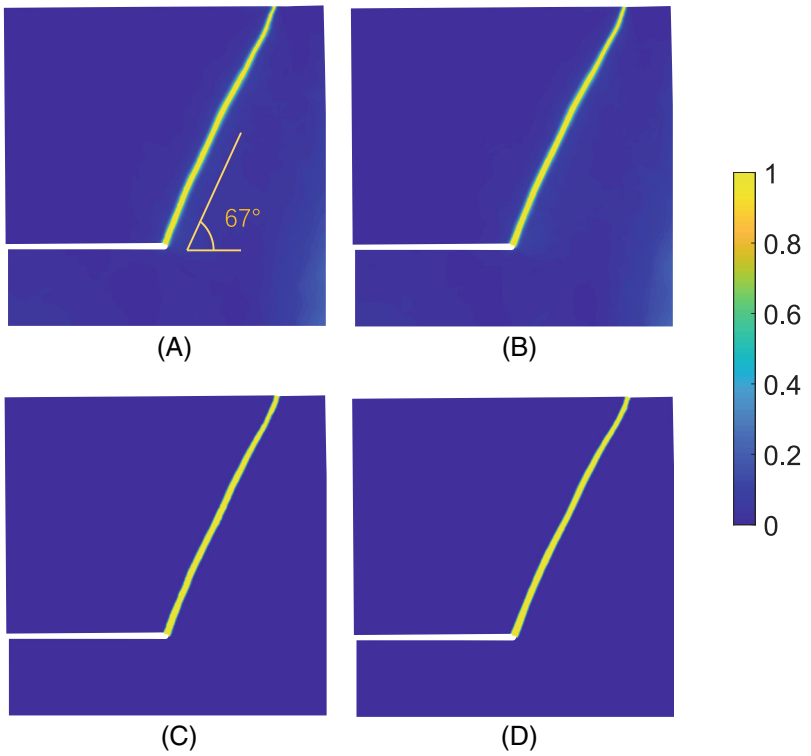

FIGURE 15 Phase field results of the test in Section 4.3 at $t = 87$ μs. (A) AT2 with $h = l/2$; (B) AT2 with $h = l/4$; (C) AT1 with $h = l/2$; (D) AT1 with $h = l/4$

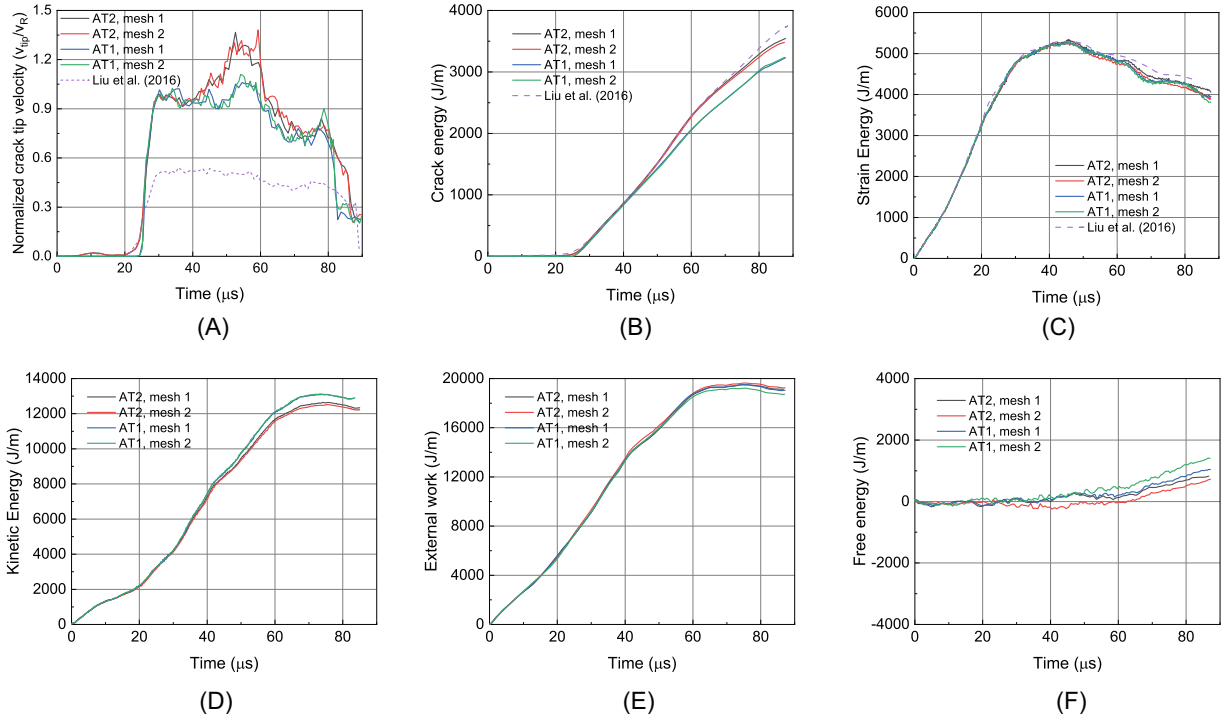

FIGURE 16 Results of the test in Section 4.3 compared with Liu et al.[54] Evolution of: (A) Normalized crack tip velocity; (B) crack energy; (C) strain energy; (D) kinetic energy; (E) external work; and (F) free energy. The external work (E) is obtained by sampling the power of the reaction force, and then integrating this power with respect to time. The free energy gradually increases, reaching between 3.74% and 7.34% of the external work in the end, which seems to violate the law of conservation of energy. See Figure 19 for a comparison.

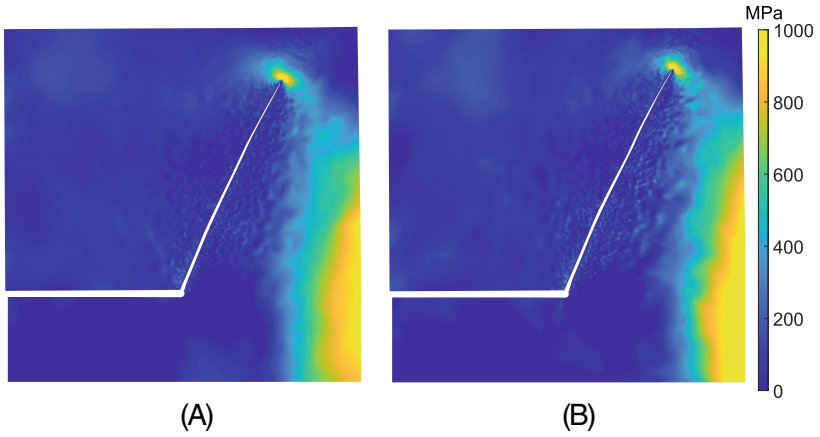

FIGURE 17 Maximum principal stress of the test in Section 4.3 with Mesh 2 at $t = 70$ μs. (A) AT2; (B) AT1

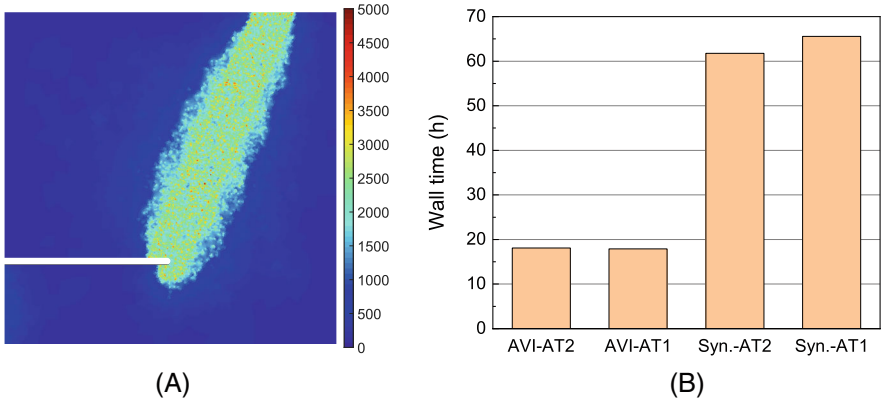

FIGURE 18 The performance indicators of the tests in Section 4.3 with Mesh 1: (A) Number of updates per element; and (B) wall time corresponding to $t_f = 87$ μs.

and the results are consistent with numerical results reported by Zhang et al.[62] Figure 16E shows the evolution of the external work, to the best of our knowledge, there is no relevant report on external work of the Kalthoff test by the phase field method at present. However, our result is in good agreement with the result using the cohesive zone model by Park et al.[63] Figure 16F shows the evolution of the free energy. As we can see, the free energy gradually increases, reaching between 715.34 and 1403.51 J at the end of the simulation, which seems to violate the law of conservation of energy. This phenomenon appears to be an open question.

Figure 17 shows the distribution of the maximum principal stress for Mesh 2. The stress concentration is clearly seen at the crack tip and the bottom right corner, in both AT2 and AT1 models. The result is in good agreement with those in Liu et al.[54]

Figure 18A shows the number of updates per element of the Kalthoff test with Mesh 1. Similar to the previous examples, the elements near the crack are updated more frequently by design while those far way are updated less frequently. Figure 18B shows the wall time corresponding to $t_f = 87$ μs, indicating that the AVI takes only one-third of the wall time of a synchronous method.

4.3.1 | Alternative method to calculate the crack tip velocity

As an attempt to reconcile the discrepancy, we employ the iso-curve strategy to calculate the crack tip velocity, as also done by Liu et al.[54] In this approach, the position of the crack tip is determined by the iso-curve with phase field $d = 0.9$. Therefore, the crack tip velocity is recalculated by $v_n = \|\boldsymbol{x}_n - \boldsymbol{x}_{n-1}\|/(t_n - t_{n-1})$, where $\boldsymbol{x}_n$ represents the location of the

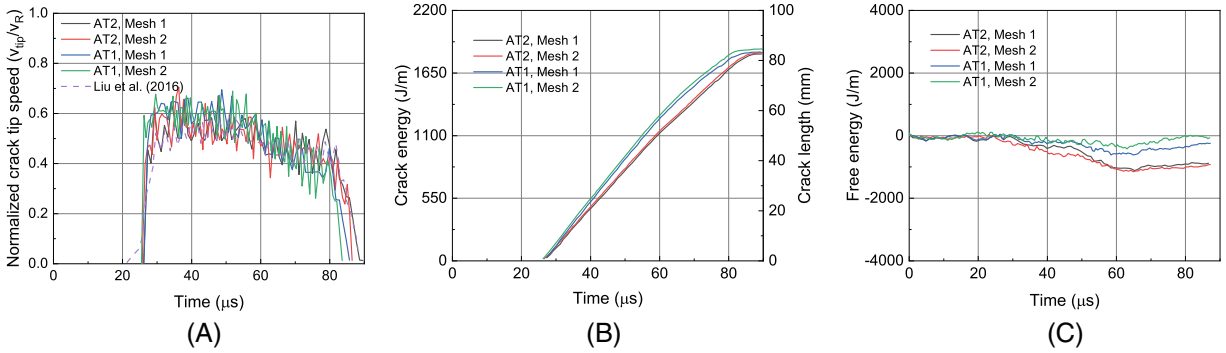

FIGURE 19 Results of the test in Section 4.3. Evolution of: (A) Normalized crack tip velocity calculated by iso-curve strategy; (B) crack energy calculated by Equation (37), that is, $\hat{\Gamma}$ (left vertical axis), and crack length (right vertical axis); and (C) free energy $T(\dot{\boldsymbol{u}}) + V(\boldsymbol{u}, d) + \hat{\Gamma}(d)$, which satisfies the conservation of energy.

crack tip at nth sampling time t_n, and the result is shown in Figure 19A. As can be seen, the crack accelerates to near $0.6v_R$ and then remains with this velocity during the propagation until it reaches the top boundary, which agrees well with the result reported in Reference 54.

With this iso-curve scheme, the four cases of Kalthoff test show a similar final crack length of approximately $l_{crack} = 83$ mm, see Figure 19B with the right vertical axis. Correspondingly, the crack energy can be computed as

$$\hat{\Gamma} = g_c l_{crack}, \tag{37}$$

with the value of 1836.79 J for a sharp crack, see Figure 19B with the left vertical axis. A significant difference is that $\hat{\Gamma}$ is much smaller than Γ, and the ratios of $\Gamma/\hat{\Gamma}$ are 1.9 and 1.75 for the AT2 and AT1 models, respectively.

In addition, we recalculate the free energy by using (37) instead of (4), that is, $T(\dot{\boldsymbol{u}}) + V(\boldsymbol{u}, d) + \hat{\Gamma}$, and the result is shown in Figure 19C. As seen, with $\hat{\Gamma}$, the results are energetically stable and satisfy the conservation of energy.

4.3.2 | Discussions

In the Kalthoff test, the crack energy calculated by (4) is higher than that by (37). This phenomenon is not unique to this work but also reported in References 22,46,54,61,62,64, and 65, in which the ratio of $\Gamma/\hat{\Gamma}$ is between 1.90 and 2.45, equal to or even higher than our value. Meanwhile, in Reference 23, this ratio is 1.37. In addition, this phenomenon was also reported in other dynamic phase field fracture by Ziaei-Rad and Shen,[27] where the ratio is approximately 2.

Although the main reason why Γ is higher than $\hat{\Gamma}$ need to be further investigated, we suggest that the way of enforcing irreversibility constraint is not an ideal candidate. Borden et al.[22] suggested that the strain-history field (alternative way to enforce the irreversibility) could play an important role, but the ratio of $\Gamma/\hat{\Gamma}$ is still 1.4 despite the strain-history field being removed which allows the crack to heal. In addition, Geelen et al.[46] employed the augmented Lagrangian method to enforce the irreversibility and the resulting ratio is 2.

Moreover, Li et al.[14] stated that the numerical phase field of the Kalthoff test is wider than the analytical one, and the wider damage profile will lead to an amplified effective fracture toughness, which had also been reported by Bourdin et al.[66] Furthermore, Bleyer et al.[67] suggested that the mesh size has an influence on the result of both quasi-static and dynamic fracture and that will further lead to an overestimated crack energy (see eqs. (16) and (17) in Reference 67 for more details).

This issue appears to be an open question for the Kalthoff test.

4.4 | The fiber-reinforced composite test

This section studies the cracking behavior in a fiber-reinforced composite with two asymmetric initial explicit cracks. Figure 20A illustrates the geometry and the boundary conditions, where the cracks are located at the end of the parallel

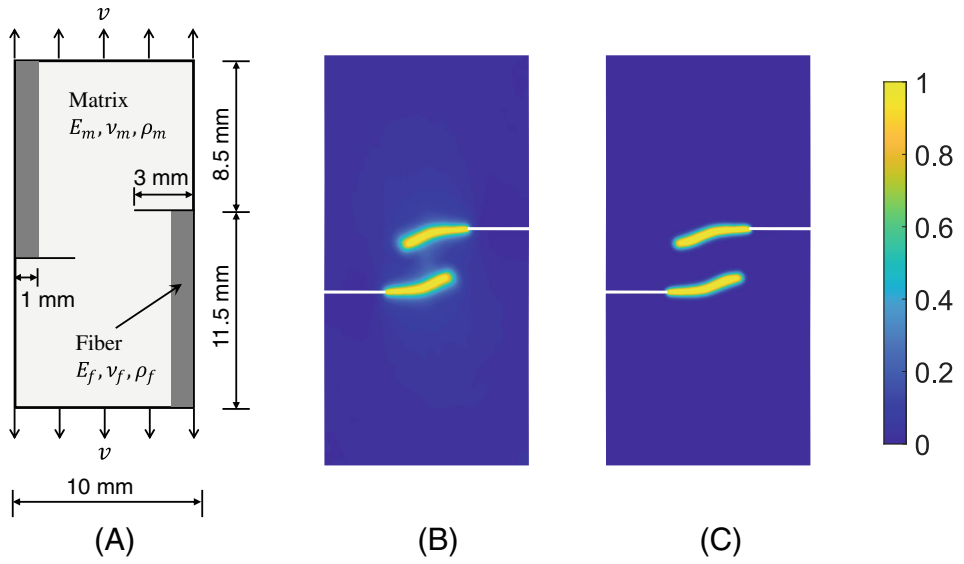

FIGURE 20 The fiber-reinforced composite test. (A) The geometry and boundary conditions, where $v = 5$ m/s. The phase field results of the (B) AT2 and (C) AT1.

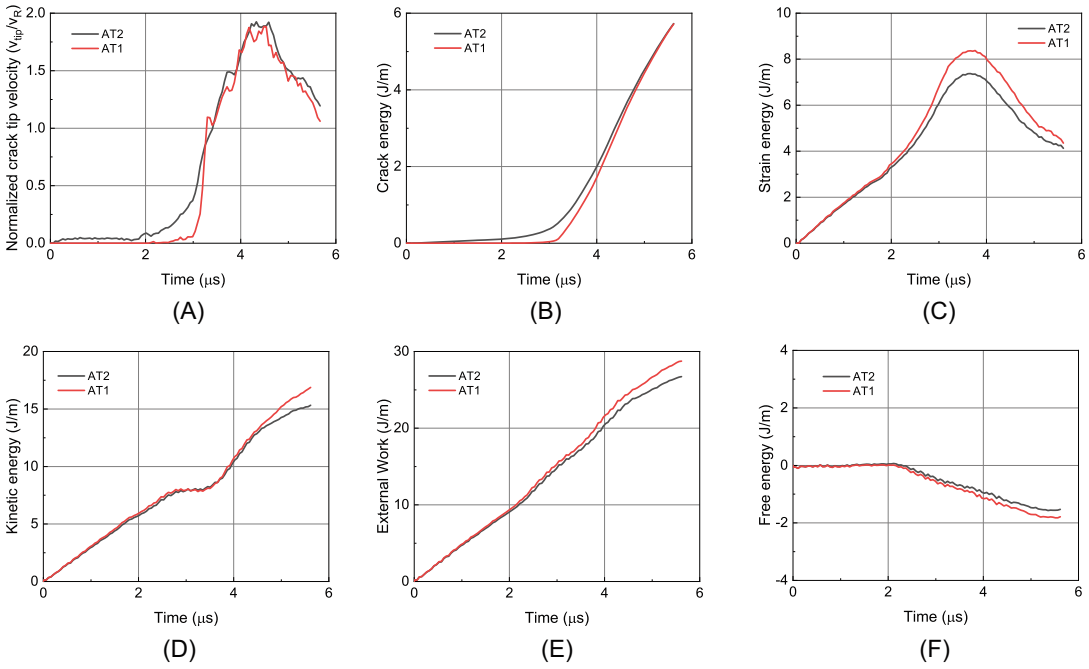

FIGURE 21 Results of the fiber-reinforced composite test in Section 4.4 as the evolution of: (A) Normalized total crack tip velocity; (B) crack energy; (C) strain energy; (D) kinetic energy; (E) external work; and (F) free energy.

fibers and with a length of 3 mm. Plane stress state is assumed. The material parameters for the matrix are selected as $E_m = 35$ GPa, $\nu_m = 0.42$, $\rho_m = 1450$ kg/m^3, $g_{cm} = 5 \times 10^2$ J/m^2, $\ell_m = 2 \times 10^{-4}$ m while those for the fiber are $E_f = 208$ GPa, $\nu_f = 0.42$, $\rho_f = 8000$ kg/m^3, $g_{cf} = 1 \times 10^4$ J/m^2, $\ell_f = 1 \times 10^{-3}$ m. The mesh size in the refined region is $h = 5 \times 10^{-5}$ m $= \ell_m/4$.

Figure 20B,C show the phase field results of the AT2 and AT1 models, respectively. It is observed that the cracks propagate from the pre-crack tips and toward each other in a curved shape. This crack pattern was also observed in References 68 and 69.

Figure 21A shows the evolution of the normalized crack tip velocity. The cracks propagate at 3 μs and rapidly increase to the Rayleigh wave speed v_R, then decrease to $v_R/2$ at the end of the simulation. Figure 21B shows the

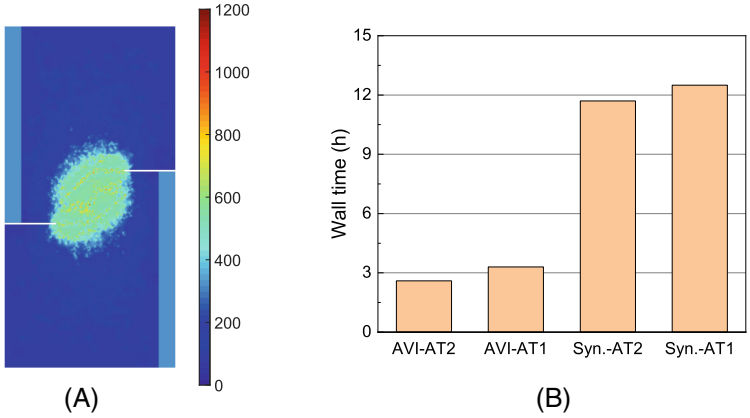

FIGURE 22 The performance indicators of the tests in Section 4.4: (A) Number of updates per element; and (B) wall time corresponding to $t_f = 5.5$ μs.

evolution of the crack energy, which increases monotonically during the simulation. Figure 21C shows the evolution of the strain energy, which increases at the beginning and then decreases after the cracks begin to propagation. Figure 21D shows the evolution of the kinetic energy. Interestingly the kinetic energy shows a plateau at the beginning of the crack propagation (about 3 μs) and then increases. Figure 21E,F show the evolution of the external work and the free energy respectively, indicating that the free energy is approximately 6% of the external work at the end of the simulation.

Figure 22A shows the number of updates per element. Again, by design, the elements near the cracks are updated more frequently. Furthermore, it is noted that the fiber elements are updated three times more frequently than the matrix elements far away from the cracks. Figure 22B shows the wall time corresponding to $t_f = 5.5$ μs for the AVI and a synchronous method, and the results indicate that the time the AVI takes is approximately a quarter times that of a synchronous method.

5 | CONCLUSIONS

In this article, we have proposed an asynchronous variational formulation for the phase field approach to dynamic brittle fracture. The formulation is derived from Hamilton's principle of stationary action and to a great extent, retains the advantages of variational integrators. A major characteristic of the formulation is that it allows elements to have independent time steps. The result indicates that the formulation is able to simulate dynamic fracture propagation and branching successfully. As a result of the variational structure, the formulation performs a remarkable energy behavior during the simulation. Compared to synchronous methods, the presented formulation is computationally more efficient for problems involving a high contrast in element sizes or material properties, such as bi-materials.

Another characteristic is that the phase field irreversibility condition is enforced by the reduced-space active set method at the level of element patches. As a result, the AT2 and AT1 variants of the phase field approach may be implemented with similar costs. The present study shows that these two variants lead to similar results at roughly the same computational cost.

ACKNOWLEDGMENTS

We acknowledge the financial support by the National Natural Science Foundation of China, Grant No. 11972227, and by the Natural Science Foundation of Shanghai, Grant No. 19ZR1424200.

DATA AVAILABILITY STATEMENT

Data sharing not applicable to this article as no datasets were generated or analyzed during the current study.

ORCID

Zongwu Niu https://orcid.org/0000-0002-5891-8338
Yongxing Shen https://orcid.org/0000-0001-9397-3853

REFERENCES

1. Yao Y, Keer LM. Cohesive fracture mechanics based numerical analysis to BGA packaging and lead free solders under drop impact. *Microelectron Reliab*. 2013;53(4):629-637. doi:10.1016/j.microrel.2012.12.007
2. Zhang R, Zhang X, Kang T, He F. Dynamic fracture propagation model for oriented perforation steering fracturing in low permeability reservoir based on microelement method. *J Nat Gas Sci Eng*. 2020;74:103105. doi:10.1016/j.jngse.2019.103105
3. Chen S, Zang M, Wang D, Yoshimura S, Yamada T. Numerical analysis of impact failure of automotive laminated glass: a review. *Compos Part B*. 2017;122:47-60. doi:10.1016/j.compositesb.2017.04.007
4. Freund LB. *Dynamic Fracture Mechanics*. Cambridge University Press; 1998.
5. Ravi-Chandar K. *Dynamic Fracture*. Elsevier; 2004.
6. Fineberg J, Bouchbinder E. Recent developments in dynamic fracture: some perspectives. *Int J Fract*. 2015;196(1-2):33-57. doi:10.1007/s10704-015-0038-x
7. Sun Y, Edwards MG, Chen B, Li C. A state-of-the-art review of crack branching. *Eng Fract Mech*. 2021;257:108036. doi:10.1016/j.engfracmech.2021.108036
8. Rabczuk T. Computational methods for fracture in brittle and quasi-brittle solids: state-of-the-art review and future perspectives. *International Scholarly Research Notices*. 2013;2013:1-38. doi:10.1155/2013/849231
9. Réthoré J, Gravouil A, Combescure A. An energy-conserving scheme for dynamic crack growth using the eXtended finite element method. *Int J Numer Methods Eng*. 2005;63(5):631-659. doi:10.1002/nme.1283
10. Nguyen VP. Discontinuous Galerkin/extrinsic cohesive zone modeling: implementation caveats and applications in computational fracture mechanics. *Eng Fract Mech*. 2014;128:37-68. doi:10.1016/j.engfracmech.2014.07.003
11. Liu Y, Filonova V, Hu N, et al. A regularized phenomenological multiscale damage model. *Int J Numer Methods Eng*. 2014;99(12):867-887. doi:10.1002/nme.4705
12. Zhang Y, Zhuang X. Cracking elements method for dynamic brittle fracture. *Theor Appl Fract Mech*. 2019;102:1-9. doi:10.1016/j.tafmec.2018.09.015
13. Song JH, Areias PMA, Belytschko T. A method for dynamic crack and shear band propagation with phantom nodes. *Int J Numer Methods Eng*. 2006;67(6):868-893. doi:10.1002/nme.1652
14. Li T, Marigo JJ, Guilbaud D, Potapov S. Gradient damage modeling of brittle fracture in an explicit dynamics context. *Int J Numer Methods Eng*. 2016;108(11):1381-1405. doi:10.1002/nme.5262
15. Moreau K, Moës N, Picart D, Stainier L. Explicit dynamics with a non-local damage model using the thick level set approach. *Int J Numer Methods Eng*. 2015;102(3-4):808-838. doi:10.1002/nme.4824
16. Bourdin B, Francfort GA, Marigo JJ. Numerical experiments in revisited brittle fracture. *J Mech Phys Solids*. 2000;48(4):797-826. doi:10.1016/S0022-5096(99)00028-9
17. Francfort GA, Marigo JJ. Revisiting brittle fracture as an energy minimization problem. *J Mech Phys Solids*. 1998;46(8):1319-1342. doi:10.1016/S0022-5096(98)00034-9
18. Amiri F, Millán D, Shen Y, Rabczuk T, Arroyo M. Phase-field modeling of fracture in linear thin shells. *Theor Appl Fract Mech*. 2014;69:102-109. doi:10.1016/j.tafmec.2013.12.002
19. Lai W, Gao J, Li Y, Arroyo M, Shen Y. Phase field modeling of brittle fracture in an Euler-Bernoulli beam accounting for transverse part-through cracks. *Comput Methods Appl Mech Eng*. 2020;361:112787. doi:10.1016/j.cma.2019.112787
20. Mollaali M, Ziaei-Rad V, Shen Y. Numerical modeling of CO2 fracturing by the phase field approach. *J Nat Gas Sci Eng*. 2019;70:102905. doi:10.1016/j.jngse.2019.102905
21. Shen Y, Mollaali M, Li Y, Ma W, Jiang J. Implementation details for the phase field approaches to fracture. *J Shanghai Jiaotong Univ (Sci)*. 2018;23(1):166-174. doi:10.1007/s12204-018-1922-0
22. Borden MJ, Verhoosel CV, Scott MA, Hughes TJ, Landis CM. A phase-field description of dynamic brittle fracture. *Comput Methods Appl Mech Eng*. 2012;217-220:77-95. doi:10.1016/j.cma.2012.01.008
23. Nguyen VP, Wu JY. Modeling dynamic fracture of solids with a phase-field regularized cohesive zone model. *Comput Methods Appl Mech Eng*. 2018;340:1000-1022. doi:10.1016/j.cma.2018.06.015
24. Hao S, Shen Y, Cheng JB. Phase field formulation for the fracture of a metal under impact with a fluid formulation. *Eng Fract Mech*. 2022;261:108142. doi:10.1016/j.engfracmech.2021.108142
25. Hao S, Chen Y, Cheng JB, Shen Y. A phase field model for high-speed impact based on the updated Lagrangian formulation. *Finite Elem Anal Des*. 2022;199:103652. doi:10.1016/j.finel.2021.103652
26. Tian F, Tang X, Xu T, Yang J, Li L. A hybrid adaptive finite element phase-field method for quasi-static and dynamic brittle fracture. *Int J Numer Methods Eng*. 2019;120(9):1108-1125. doi:10.1002/nme.6172
27. Ziaei-Rad V, Shen Y. Massive parallelization of the phase field formulation for crack propagation with time adaptivity. *Comput Methods Appl Mech Eng*. 2016;312:224-253. doi:10.1016/j.cma.2016.04.013
28. Li Y, Lai W, Shen Y. Variational h-adaption method for the phase field approach to fracture. *Int J Fract*. 2019;217:83-103. doi:10.1007/s10704-019-00372-y
29. Engwer C, Pop IS, Wick T. Dynamic and weighted stabilizations of the L-scheme applied to a phase-field model for fracture propagation; 2021:1177-1184; Springer International Publishing, Cham.
30. Lew A, Marsden JE, Ortiz M, West M. Asynchronous variational integrators. *Arch Ration Mech Anal*. 2003;167(2):85-146. doi:10.1007/s00205-002-0212-y
31. Lew A, Marsden JE, Ortiz M, West M. Variational time integrators. *Int J Numer Methods Eng*. 2004;60(1):153-212. doi:10.1002/nme.958

32. Fong W, Darve E, Lew A. Stability of asynchronous variational integrators. *J Comput Phys*. 2008;227(18):8367-8394. doi:10.1016/j.jcp.2008.05.017
33. Focardi M, Mariano PM. Convergence of asynchronous variational integrators in linear elastodynamics. *Int J Numer Methods Eng*. 2008;75(7):755-769. doi:10.1002/nme.2271
34. Ryckman RA, Lew AJ. An explicit asynchronous contact algorithm for elastic body-rigid wall interaction. *Int J Numer Methods Eng*. 2012;89(7):869-896. doi:10.1002/nme.3266
35. Liu P, Yang JZ, Yuan C. Extended synchronous variational integrators for wave propagations on non-uniform meshes. *Commun Comput Phys*. 2020;28(2):691-722. doi:10.4208/cicp.OA-2019-0167
36. Thomaszewski B, Pabst S, Straßer W. Asynchronous cloth simulation. Proceedings of the 2008 International Conference on Computer Graphics and Virtual Reality; 2008.
37. Pham K, Amor H, Marigo JJ, Maurini C. Gradient damage models and their use to approximate brittle fracture. *Int J Damage Mech*. 2011;20(4):618-652. doi:10.1177/1056789510386852
38. Ren HL, Zhuang X, Anitescu C, Rabczuk T. An explicit phase field method for brittle dynamic fracture. *Comput Struct*. 2019;217:45-56. doi:10.1016/j.compstruc.2019.03.005
39. Suh HS, Sun W. Asynchronous phase field fracture model for porous media with thermally non-equilibrated constituents. *Comput Methods Appl Mech Eng*. 2021;387:114182. doi:10.1016/j.cma.2021.114182
40. Miehe C, Hofacker M, Welschinger F. A phase field model for rate-independent crack propagation: robust algorithmic implementation based on operator splits. *Comput Methods Appl Mech Eng*. 2010;199(45):2765-2778. doi:10.1016/j.cma.2010.04.011
41. Amor H, Marigo JJ, Maurini C. Regularized formulation of the variational brittle fracture with unilateral contact: numerical experiments. *J Mech Phys Solids*. 2009;57(8):1209-1229. doi:10.1016/j.jmps.2009.04.011
42. Liu Y, Cheng C, Ziaei-Rad V, Shen Y. A micromechanics-informed phase field model for brittle fracture accounting for unilateral constraint. *Eng Fract Mech*. 2021;241:107358. doi:10.1016/j.engfracmech.2020.107358
43. Wu JY, Nguyen VP, Zhou H, Huang Y. A variationally consistent phase-field anisotropic damage model for fracture. *Comput Methods Appl Mech Eng*. 2020;358:112629. doi:10.1016/j.cma.2019.112629
44. Marsden JE, West M. Discrete mechanics and variational integrators. *Acta Numer*. 2001;10(10):357-514. doi:10.1017/S096249290100006X
45. Gerasimov T, De Lorenzis L. On penalization in variational phase-field models of brittle fracture. *Comput Methods Appl Mech Eng*. 2019;354:990-1026. doi:10.1016/j.cma.2019.05.038
46. Geelen RJM, Liu Y, Hu T, Tupek MR, Dolbow JE. A phase-field formulation for dynamic cohesive fracture. *Comput Methods Appl Mech Eng*. 2019;348:680-711. doi:10.1016/j.cma.2019.01.026
47. Wu JY. Robust numerical implementation of non-standard phase-field damage models for failure in solids. *Comput Methods Appl Mech Eng*. 2018;340:767-797. doi:10.1016/j.cma.2018.06.007
48. Farrell P, Maurini C. Linear and nonlinear solvers for variational phase-field models of brittle fracture. *Int J Numer Methods Eng*. 2017;109(5):648-667. doi:10.1002/nme.5300
49. Knuth DE. *The Art of Computer Programming*. Addison Wesley; 1998.
50. Song JH, Wang H, Belytschko T. A comparative study on finite element methods for dynamic fracture. *Comput Mech*. 2008;42:239-250. doi:10.1007/s00466-007-0210-x
51. Ramulu M, Kobayashi AS. Mechanics of crack curving and branching – A dynamic fracture analysis. *Int J Fract*. 1985;27:187-201. doi:10.1007/BF00017967
52. Sharon E, Fineberg J. Microbranching instability and the dynamic fracture of brittle materials. *Phys Rev B Condens Matter*. 1996;54(10):7128-7139. doi:10.1103/physrevb.54.7128
53. Schlüter A, Kuhn C, Müller R. Phase field approximation of dynamic brittle fracture. *Proc Appl Math Mech*. 2014;14(1):143-144. doi:10.1002/pamm.201410059
54. Liu G, Li Q, Msekh MA, Zuo Z. Abaqus implementation of monolithic and staggered schemes for quasi-static and dynamic fracture phase-field model. *Comput Mater Sci*. 2016;121:35-47. doi:10.1016/j.commatsci.2016.04.009
55. Bobaru F, Zhang G. Why do cracks branch? A peridynamic investigation of dynamic brittle fracture. *Int J Fract*. 2015;196:59-98. doi:10.1007/s10704-015-0056-8
56. Mandal TK, Nguyen VP, Wu JY. Evaluation of variational phase-field models for dynamic brittle fracture. *Eng Fract Mech*. 2020;235:107169. doi:10.1016/j.engfracmech.2020.107169
57. Kalthoff JF. Shadow optical analysis of dynamic shear fracture. *Opt Eng*. 1988;27(10):835-840. doi:10.1117/12.7976772
58. Kalthoff JF. Modes of dynamic shear failure in solids. *Int J Fract*. 2000;101(1):1-31. doi:10.1023/A:1007647800529
59. Wang H, Xu Y, Huang D. A non-ordinary state-based peridynamic formulation for thermo-visco-plastic deformation and impact fracture. *Int J Mech Sci*. 2019;159:336-344. doi:10.1016/j.ijmecsci.2019.06.008
60. Chu D, Li X, Liu Z. Study the dynamic crack path in brittle material under thermal shock loading by phase field modeling. *Int J Fract*. 2017;208:115-130. doi:10.1007/s10704-017-0220-4
61. Zhou S, Rabczuk T, Zhuang X. Phase field modeling of quasi-static and dynamic crack propagation: COMSOL implementation and case studies. *Adv Eng Softw*. 2018;122:31-49. doi:10.1016/j.advengsoft.2018.03.012
62. Zhang Y, Ren H, Areias P, Zhuang X, Rabczuk T. Quasi-static and dynamic fracture modeling by the nonlocal operator method. *Eng Anal Bound Elem*. 2021;133:120-137. doi:10.1016/j.enganabound.2021.08.020
63. Park K, Paulino GH, Celes W, Espinha R. Adaptive mesh refinement and coarsening for cohesive zone modeling of dynamic fracture. *Int J Numer Methods Eng*. 2012;92(1):1-35. doi:10.1002/nme.3163

64. Tangella RG, Kumbhar P, Annabattula RK. Hybrid phase field modelling of dynamic brittle fracture and implementation in FEniCS. In: Krishnapillai SRV, Ha SK, eds. *Composite Materials for Extreme Loading*. Springer; 2022:15-24.
65. Reddy SSK, Amirtham R, Reddy JN. Modeling fracture in brittle materials with inertia effects using the phase field method. *Mech Adv Mater Struct*. 2021. doi:10.1080/15376494.2021.2010289
66. Bourdin B, Francfort GA, Marigo JJ. The variational approach to fracture. *J Elast*. 2008;91:5-148. doi:10.1007/s10659-007-9107-3
67. Bleyer J, Roux-Langlois C, Molinari JF. Dynamic crack propagation with a variational phase-field model: limiting speed, crack branching and velocity-toughening mechanisms. *Int J Fract*. 2017;204:79-100. doi:10.1007/s10704-016-0163-1
68. Yin BB, Zhang LW. Phase field method for simulating the brittle fracture of fiber reinforced composites. *Eng Fract Mech*. 2019;211:321-340. doi:10.1016/j.engfracmech.2019.02.033
69. Sumi Y, Wang ZN. A finite-element simulation method for a system of growing cracks in a heterogeneous material. *Mech Mater*. 1998;28(1):197-206. doi:10.1016/S0167-6636(97)00048-3

How to cite this article: Niu Z, Ziaei-Rad V, Wu Z, Shen Y. An asynchronous variational integrator for the phase field approach to dynamic fracture. *Int J Numer Methods Eng*. 2023;124(2):434-457. doi: 10.1002/nme.7127

APPENDIX A. THE CASE WITH COINCIDENCE IN THE UPDATE SCHEDULE

The assumption of no coincident instants is not a restrictive assumption but for simplifying the derivation. Without this assumption, consider the case in which there are coincidences in the update instants for multiple adjacent elements sharing node a. Let the set of these nodes be denoted $\mathcal{T}_a$. It can be shown that the result of the simulation is equal for the pure elasticity case even if the update order of the elements in $\mathcal{T}_a$ is exchanged.

However, when considering the phase field, the results are slightly dependent on the update order due to the irreversibility of the phase field. An alternative and the most orthodox treatment is to rewrite (24) as

$$0 = \frac{\partial S_{dis}}{\partial \mathbf{u}_a^i} = \frac{\partial}{\partial \mathbf{u}_a^i}\left(\frac{1}{2}M_a\left(t_a^i - t_a^{i-1}\right)\left\|\frac{\mathbf{u}_a^i - \mathbf{u}_a^{i-1}}{t_a^i - t_a^{i-1}}\right\|^2 + \frac{1}{2}M_a\left(t_a^{i+1} - t_a^i\right)\left\|\frac{\mathbf{u}_a^{i+1} - \mathbf{u}_a^i}{t_a^{i+1} - t_a^i}\right\|^2 - \sum_{e\in\mathcal{T}_a}\left(t_e^j - t_e^{j-1}\right)V_e\left(\mathbf{u}_e^j, \mathbf{d}_e^j\right)\right),$$

with the last term modified compared with (24). In this treatment, the elements in $\mathcal{T}_a$ need to be simultaneously updated. It is believed that such more rigorous treatment will not alter too much the numerical results.

APPENDIX B. PHASE FIELD RESULT WITHOUT USING ELEMENT PATCHES

Figure B1 shows the phase field result obtained with (28), that is, without patches, the boundary conditions and material properties are the same as those of Section 4.1. As seen, the crack patterns are too diffused.

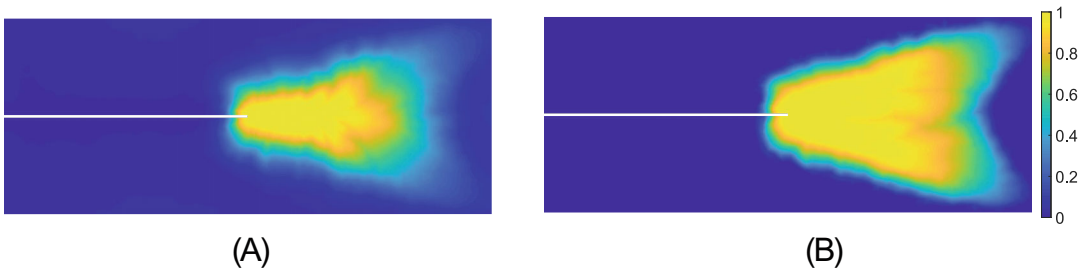

FIGURE B1 Phase field result with the formulation without using patches. (A) AT2; (B) AT1